Structure and Evolution of the 22 February 1993 TOGA COARE Squall Line: Organization Mechanisms Inferred from Numerical Simulation

STANLEY B. TRIER, WILLIAM C. SKAMAROCK, AND MARGARET A. LEMONE

National Center for Atmospheric Research, Boulder, Colorado*

(Manuscript received 29 February 1996, in final form 17 July 1996)

ABSTRACT

Mechanisms responsible for meso- and convective-scale organization within a large tropical squall line that occurred on 22 February 1993 during the Tropical Ocean Global Atmosphere Coupled Ocean–Atmosphere Response Experiment are investigated using a three-dimensional numerical cloud model. The squall line occurred in an environment typical of fast-moving tropical squall lines, characterized by moderate convective available potential energy and moderate-to-strong vertical shear beneath a low-level jet with weak reverse vertical shear above.

A well-simulated aspect of the observed squall line is the evolution of a portion of its leading convective zone from a quasi-linear to a three-dimensional bow-shaped structure over a 2-h period. This transition is accompanied by the development of both a prominent mesoscale vortex along the northern edge of the 40–60-km long bow-shaped feature and elongated bands of weaker reflectivity situated rearward and oriented transverse to the leading edge, within enhanced front-to-rear system relative midlevel flow, near the southern end of the bow. The vertical wind shear that arises from the convectively induced mesoscale flow within the squall-line system is found to be a critical factor influencing 1) the development of the vortex and 2) through its associated vertical pressure gradients, the pronounced along-line variability of the convective updraft and precipitation structure. The environmental wind profile is also critical to system organization since the orientation of its vertical shear (in layers both above and below the environmental jet height) relative to the local orientation of the incipient storm-induced subcloud cold pool directly influences the onset of the convectively induced mesoscale flow.

1. Introduction

This paper represents the second part of a study in which we report on numerical simulations of a large mesoscale convective system (MCS) that occurred on 22 February 1993 over the equatorial western Pacific Ocean during the Tropical Ocean Global Atmosphere (TOGA) Coupled Ocean–Atmosphere Response Experiment (COARE). The first part of this study (Trier et al. 1996) examined the sensitivity of convective organization and short-term ($t \leq 6$ h) MCS evolution to small-scale physical processes including ice microphysics and MCS-induced surface fluxes. In the current paper we examine the dynamics responsible for mesoscale evolution and convective organization within the precipitation system.

The simulated MCS is compared to aircraft observations in Trier et al. (1996), and a more comprehensive analysis of the observed MCS is presented in a companion paper (Jorgensen et al. 1997). This MCS is a fast-moving tropical squall line maintained by lifting of conditionally unstable environmental air by its downdraft-induced subcloud cold pool. Structural features discussed in these papers include 1) a characteristic rearward tilting convective zone found over a large portion of the squall line, which, when averaged in the along-line direction, consisted of a shallow leading edge updraft maximum followed by a midtropospheric minimum in vertical velocity ahead of an upper-tropospheric updraft maximum; 2) a mesoscale convectively generated vortex (MCV) that develops in association with the transition of a portion of the leading-edge convective band from a quasi-linear to a bow-shaped structure; and 3) the development of elongated precipitation bands situated rearward and oriented transverse to the leading edge of the MCS during its bow-shaped stage.

Trier et al. (1996) found that ice microphysics and surface fluxes were not needed to simulate general characteristics of these observed features. However, inclusion of such processes resulted in simulated structures that most closely resembled observations and also im-

---

* The National Center for Atmospheric Research is sponsored by the National Science Foundation.

[1] The scientific objectives of TOGA COARE are discussed in Webster and Lukas (1992).

Corresponding author address: Stanley B. Trier, National Center for Atmospheric Research, P. O. Box 3000, Boulder, CO 80307-3000.
E-mail: trier@ncar.ucar.edu

pacted the timing of squall-line evolution. In the current study, we continue to examine the control simulation (CONTRL) from Trier et al. (1996), which includes the effects of MCS-induced surface fluxes and ice microphysics, and exploit the superior temporal and spatial resolution afforded by the numerical model to better understand the nature of the observed features. Using trajectory analysis, we devote particular attention to mechanisms influencing MCV development and the systematic variation of convective updraft structure along the leading edge of the MCS.

Previous numerical studies (Thorpe et al. 1982; Rotunno et al. 1988) have discussed how the interaction of the environmental vertical shear with the subcloud cold pool is fundamental to the sustenance of deep convection at the leading edge of fast-moving squall lines. Other studies (e.g., Lafore and Moncrieff 1989; Weisman 1992, 1993) have since clarified how the structure and intensity of deep convection, governed primarily by these inherently two-dimensional mechanisms, can be substantially modified in mature stages of squall lines by convectively induced mesoscale circulations.

In the current fully three-dimensional numerical study we extend the results of previous numerical studies, which have been primarily two-dimensional or quasi-three-dimensional (subject to the boundary constraint of along-line periodicity), by illustrating how the *local* orientation of the arc-shaped cold pool relative to the environmental vertical wind shear can impact the convectively induced mesoscale flow field. We then show how these mesoscale flows and their associated vertical pressure gradients modulate the dynamics of deep convection as the squall-type MCS matures and are associated with variations in the convective updraft structure along the leading edge of the MCS.

MCVs often constitute a major component of the mesoscale internal circulation that develops as MCSs mature. In the current case, the stronger and more well defined vortex at the northern end of the bow-shaped convective segment was sampled by airborne Doppler radar for a ~2 h period (Jorgensen et al. 1997), during which its size and location relative to the leading convective band was similar to the line-end vortices simulated by Weisman (1993). Previous studies have illustrated that tilting of either the environmental (Weisman 1993) or MCS-generated (Davis and Weisman 1994a, b; Skamarock et al. 1994) vertical shear can be influential in the initiation of these vortices. Convergence of both relative vorticity and, in the later stages, planetary vorticity (Davis and Weisman 1994a; Skamarock et al. 1994) can result in the instensification and growth in scale of this type of vortex. In the current study, we demonstrate that MCS-induced vertical shear, which arises from horizontal gradients of buoyancy near the cold pool–updraft interface, is a major source of horizontal vorticity that is tilted and stretched during the development of the simulated northern vortex.

The paper is organized as follows. In section 2 we discuss conditions observed in the environment of the MCS and briefly describe the numerical model used to simulate deep convection. The mesoscale structure and evolution of the precipitation system is described in section 3. The structure and dynamics of the convective updrafts and mesoscale vortices are then examined in sections 4 and 5, respectively. Salient results are summarized and discussed further in section 6. A unifying theme that emerges from this analysis is that the observed features, including updraft structure and the development of mesoscale vortices and subsequent elongated transverse precipitation bands, are each manifestations of the effect of strong vertical shear that develops in association with the mesoscale pressure and horizontal flow perturbations of the evolving MCS.

2. Environmental conditions and numerical model

Deep convection is simulated for 6 h using a three-dimensional nonhydrostatic primitive equation model that employs the automated adaptive grid algorithms described in Skamarock (1989) and Skamarock and Klemp (1993). Because of the relatively short duration of the simulation and the location of the observed MCS at low latitudes (9°–10°S), neither the Coriolis force nor radiative effects are included. This version of the numerical model contains a bulk microphysical parameterization (Rutledge and Hobbs 1984) that includes a three-class (graupel, snow, and cloud ice) ice scheme. The effects of MCS-induced surface fluxes of heat, moisture, and momentum are also represented. To avoid unrealistic evolution of the MCS environment, the surface fluxes associated with the base state are not included as forcing since effects that compensate these fluxes are not present in the current model framework. A more complete description of these physical parameterizations, the model domain, and boundary conditions is provided in Trier et al. (1996).

The environment in advance of the MCS is consistent with conditions found ahead of previously documented fast-moving tropical squall lines (e.g., Barnes and Sieckman 1984). The vertical thermodynamic structure (Fig. 1a) is conditionally unstable with convective available potential energy (CAPE) of ~1500 J kg^{-1} for irreversible pseudoadiabatic ascent of a surface-based air parcel averaged through the lowest 50 mb. The environmental hodograph (Fig. 1b) features a 12 m s^{-1} jet at 2 km MSL. The jet profile leads to a moderate-to-strong component of low-level vertical shear normal to the mean orientation of the leading edge of the MCS with weak reverse vertical shear above the jet axis. Both the observed and simulated MCSs move at approximately the speed of the low-level jet, similar to the ‘‘critical’’ or ‘‘balanced’’ case for northern Australian squall-type systems (Keenan and Carbone 1992).

Deep convection is initiated in the numerical simulation by placing a finite surface-based cold pool at $t = 0$ in the otherwise horizontally homogeneous model do-

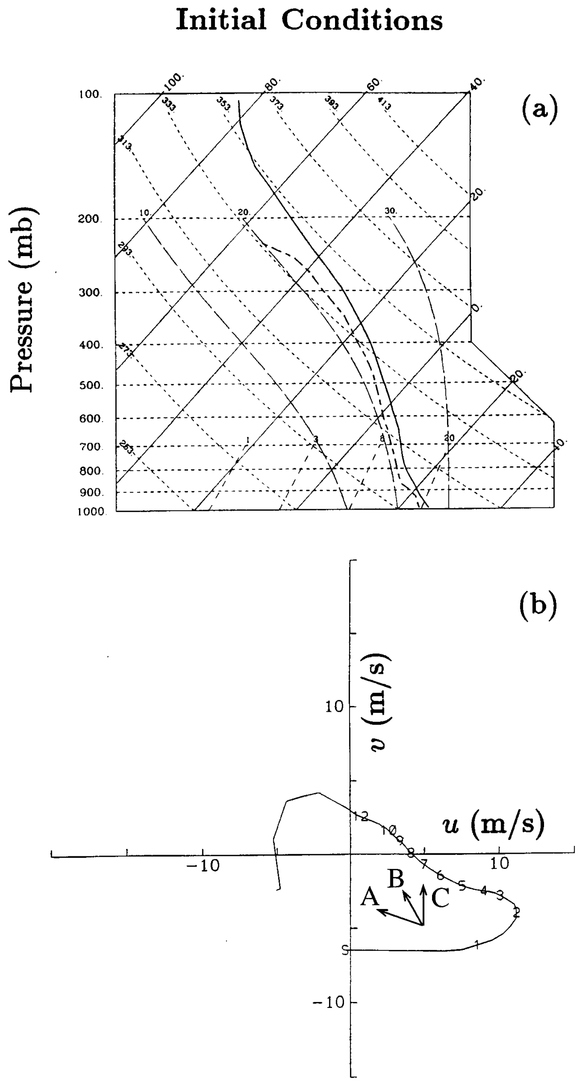

FIG. 1. (a) Temperature (solid) and dewpoint (dashed) curves in degrees Celsius and (b) hodograph (m s^{-1}) used to specify the initial condition in the numerical model. Arrows denoted by A, B, and C are oriented 90° to the left of vectors directed outward from the local orientation of the subcloud cold pool at the indicated locations in Fig. 3a. Heights (km) are annotated on the hodograph. This sounding is tabulated in the appendix of Trier et al. (1996).

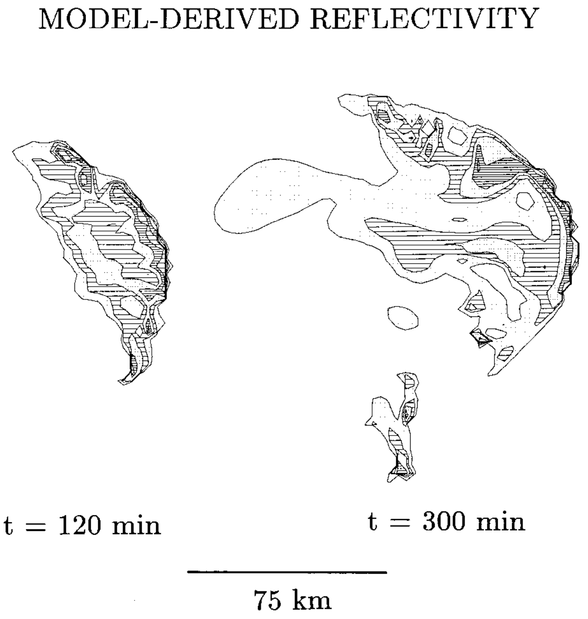

FIG. 2. Simulated radar reflectivity at 1 km MSL estimated from model-predicted bulk microphysical variables at 120 and 300 min. Shading intervals are 15–30 (dots), 30–38 (lines), 38–45 (dense dots), 45–50 (dense lines), and ≥50 dBZ (lines). A more detailed evolution from 2 to 6 h is presented in the top panel of Fig. 3 from Trier et al. (1996).

main specified by the environmental sounding (Fig. 1). A detailed explanation of both the data sources used to construct the environmental sounding and the cold pool initialization procedure is provided in Trier et al. (1996).

3. Mesoscale pressure and flow structure within the MCS

The mesoscale evolution of the simulated precipitation system is broadly similar to that of previous numerically simulated bow echoes (e.g., Weisman 1993). At 120 min, a solid band of deep convection assumes a nearly linear orientation near the front portion of a 100-km long precipitation arc (Fig. 2). Near the center of the arc, the leading-edge convection evolves into a 40–60-km long bow-shaped structure during the following 3 h. Concurrent with this evolution, mesoscale vortices develop at both the northern and southern ends of the bow-shaped precipitation feature. We focus our analysis on the region of the evolving bow-shaped feature and the nearby north flank of the larger-scale precipitation arc that continues to its northwest (Fig. 2). In this section we illustrate the spatial variability of the internal mesoscale flow and pressure fields that, in turn, strongly modulate the structure of deep convection (section 4).

As found in previous observational (LeMone et al. 1984a) and numerical (Lafore and Moncrieff 1989; Weisman 1992) studies of squall-type convective systems, mesoscale circulation begins as deep convection near the leading edge of the MCS acquires a rearward tilt. Rotunno et al. (1988) explained that rearward tilt may commence when the downdraft-induced cold pool of the incipient MCS intensifies to the extent that the low-level horizontal vorticity associated with horizontal buoyancy gradients at the cold-pool edge exceeds that associated with the ambient vertical shear, which is of the opposite sense. In contrast to this mechanism, which requires generation of horizontal vorticity, rearward tilt can also occur or be enhanced as a result of the updraft being embedded within an environmental reverse vertical shear (e.g., Malkus 1952; LeMone et al. 1984b).

As rearward tilt ensues, the vertical gradients in buoyancy that result from the positively buoyant updraft overlying the negatively buoyant cold pool are associated with a mesoscale zone of low pressure. The horizontal pressure gradients associated with the mesolow may then subsequently enhance the system-relative flows within the MCS as it matures (e.g., LeMone 1983; Smull and Houze 1987; Lafore and Moncrieff 1989). In their two-dimensional numerical simulations, Szeto and Cho (1994) found that the transition to an MCS with substantial upshear tilt and strong system-relative mesoscale flows occurs more rapidly in environments that possess reverse vertical shear above a low-level jet.

In the current simulation, early differences in midlevel front-to-rear flow and distribution of positive buoyancy[2]

$$B = g\left(\frac{\theta'}{\overline{\theta}(z)} + 0.61q_v' - q_c - q_r - q_i - q_s - q_g\right) \tag{1}$$

along the length of the MCS (Fig. 3c), which become more pronounced during the bow-echo stage (Fig. 3d), are consistent with both differences in the strength of the storm-induced cold pool and its local orientation relative to the environmental vertical shear. Along the north flank of the MCS near A (Fig. 3a), the cold pool is relatively weak and the environmental reverse vertical shear above the jet is parallel to the cold-pool orientation (Fig. 1b). Both of these factors hinder development of rearward tilt. Thus, mesoscale zones of midlevel front-to-rear flow and positive buoyancy do not develop rearward of the deep convection in this location (Figs. 3c,d). In contrast, a broad zone of midlevel positive buoyancy and front-to-rear flow develops rearward of the central convective segment at B and C (Figs. 3c,d). Here, the subcloud cold pool is stronger (Fig. 3a), which promotes rearward tilt through horizontal vorticity generation, and a significant component of the system-relative environmental flow above the jet is directed rearward, perpendicular to the local orientation of the cold pool (Fig. 1b), which may enhance the rearward tilt.

The curvature in the environmental wind profile allows for identical low-level line-normal vertical shear at B and C with significant differences in the magnitude of the line-normal reverse vertical shear aloft. The ambient vertical shear direction within the 0–2-km layer beneath the jet is 15° to the left of normal to the cold-pool edge at C (Figs. 1b, 3a) and 15° to the right of the cold-pool edge at B (Figs. 1b, 3a), resulting in identical vertical shear beneath the jet of 5.8 m s^{-1} km^{-1} normal to the leading edge of the cold pool at these locations. The negative buoyancies within the cold pool are also of comparable strength (Fig. 3a), suggesting that a similar low-level horizontal vorticity balance may hold at B and C. However, the magnitude of the environmental reverse vertical shear in the 4–7-km layer normal to the cold pool at C is -1.5 m s^{-1} km^{-1} versus only -0.9 m s^{-1} km^{-1} at B (Fig. 1b), implying a greater tendency for updrafts to develop rearward tilt at C, consistent with the more rapid onset of strong front-to-rear flow and mesoscale positive buoyancy behind C (Fig. 3c).

The buoyancy and flow fields are associated with pressure perturbations that strongly impact the organization of deep convection. To illustrate the close relationship between the midlevel pressure perturbations and the buoyancy and flow within the MCS, we follow Klemp and Rotunno (1983) and solve the following equations:

$$\boldsymbol{\nabla}\cdot(\overline{\rho}\overline{\theta}_v\boldsymbol{\nabla}\pi_{\mathrm{dn}}) = -\boldsymbol{\nabla}\cdot(\overline{\rho}\mathbf{v}\cdot\boldsymbol{\nabla}\mathbf{v}) \tag{2}$$

and

$$\boldsymbol{\nabla}\cdot(\overline{\rho}\overline{\theta}_v\boldsymbol{\nabla}\pi_{\mathrm{b}}) = \frac{\partial(\overline{\rho}B)}{\partial z} \tag{3}$$

for the components of the nondimensional pressure perturbation π (Klemp and Wilhelmson 1978) associated with spatial variations in the flow (dynamic pressure π_{dn}) and vertical gradients of buoyancy (buoyancy pressure π_{b}) over a 100 × 100 km^2 model subdomain that includes the leading convective region. For inviscid, anelastic flow, the sum of these two components constitutes the total nondimensional pressure perturbation. In (2) and (3), $\overline{\rho}$, $\overline{\theta}_v$, and $\mathbf{v}$, respectively, represent the initial density and virtual potential temperature (which are only functions of height) and the vector velocity.

The larger-scale structure of the pressure perturbation (Figs. 4a,d) closely matches that associated with the buoyancy pressure (Figs. 4b,e) and is consistent with the rearward spreading of the positively buoyant air in the front-to-rear flow (Figs. 3c,d) above the strengthening cold pool (Figs. 3a,b). The mesoscale zone of low pressure just behind the leading edge of the MCS is initially centered behind C (Fig. 4b), where the buoyancy above is strongest (Fig. 3c). Intensification and growth in scale of the front-to-rear flow then occurs as the mesolow, which itself is reinforced by this flow through the redistribution of buoyancy, expands rearward (cf. Figs. 4b,e). During the transition to a bow-shaped central convective segment, dynamic lowering of pressure associated with mesoscale organization of vertical vorticity near its ends (Fig. 4f) significantly enhances the mesolow as was also found by Weisman (1993) in simulations of larger-CAPE midlatitude bow echoes. Along the north flank of the MCS near A, where the environmental flow above the jet is parallel to the relatively weak cold pool (Fig. 1b), buoyancy remains collocated with convective updraft cores (Figs. 3c,d) and

---

[2] The buoyancy, as defined in (1), is associated with potential temperature θ and water vapor q_v departures from the horizontally homogeneous initial state, and negative contributions due to cloud water q_c, cloud ice q_i, rain q_r, snow q_s, and graupel q_g.

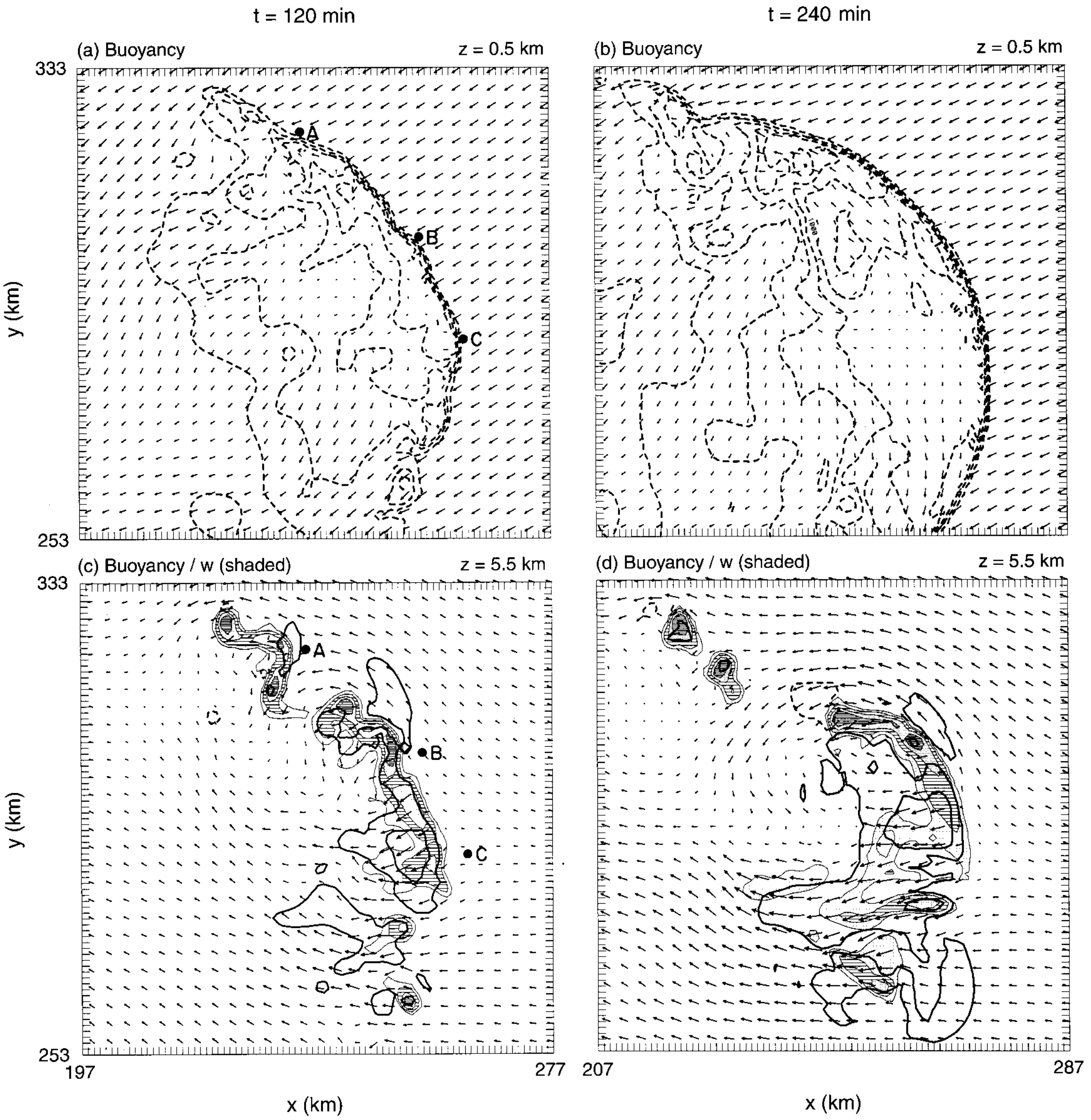

FIG. 3. Buoyancy contoured in intervals of 0.02 m s^{-2} (negative values dashed, zero contour omitted) at 0.5 km MSL for (a) 120 min and (b) 240 min, and at 5.5 km MSL for (c) 120 min and (d) 240 min. System-relative wind vectors are plotted every third model grid point with a vector length of one grid box equivalent to 5 m s^{-1}. For parts (c) and (d), vertical velocity at 5.5 km MSL is shaded in intervals of 1–2.5 (dots), 2.5–5 (lines), 5–7.5 (dense dots), and $\geq$ 7.5 m s^{-1} (dense lines).

a buoyancy-driven mesolow does not develop (Figs. 4b,e).

4. Dynamics of convective updrafts

The convective updraft structure during the early stages of the simulated MCS is similar to observations of this case (Jorgensen et al. 1997) and other tropical squall lines that occur in low-level jet environments with moderate CAPE (e.g., Roux et al. 1984; Roux 1985; Chong et al. 1987). At 2 h, a narrow zone of continuous and strong low-level updraft (contoured in Fig. 5) is present just above the leading edge of the strongest portion of the cold pool. Updrafts in the middle troposphere (shaded in Fig. 5) and upper troposphere (not shown) that are situated to the rear of the leading edge are more cellular. Along the north flank of the leading edge, strong low-level updraft maxima also occur but are less widespread. By 4 h, the midlevel updraft structure near the center portion of the leading edge has evolved into a bow morphology (Fig. 5). By this time there is greater along-line variability of rearward tilt within the leading-edge convective zone, as evidenced by differences in rearward displacement of the midlevel updrafts from low-level updrafts, along the length of the MCS.

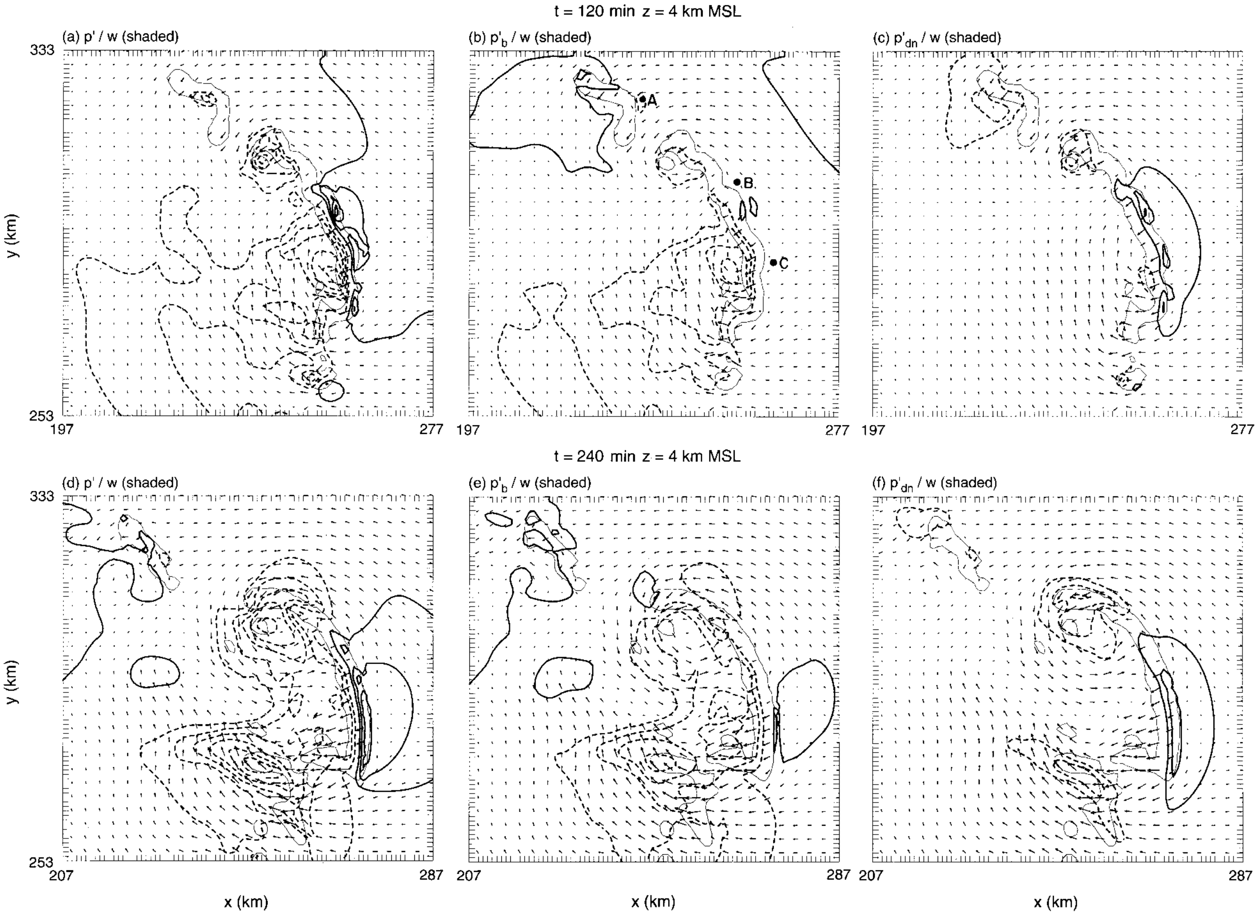

FIG. 4. The 4-km MSL total pressure perturbation p', (a) and (d); buoyancy pressure perturbations p_b', (b) and (e); and dynamic pressure perturbation p_d', (c) and (f) at 120 and 240 min. In each panel the nondimensional pressure perturbations π' are converted to dimensional units p' (0.1-mb contour intervals negative values dashed) for display. Horizontal subdomains and system-relative wind plotting conventions are as in Fig. 3. Vertical velocity at 4 km MSL is shaded where $w \geq 1$ m s^{-1}.

a. Variation of updraft structure along the MCS leading edge

Differences in the behavior of convection along the north flank and central portion of the MCS (henceforth referred to as the center line region) are quantified for the 2-h period by time series of maximum lower- (2 km MSL), middle- (7 km MSL), and upper- (12 km MSL) tropospheric updraft strength within the 15 km by 40 km rectangles[3] indicated in Fig. 5. The time series for the north flank (Fig. 6a) captures two full cycles of transient updraft areas. The development of each center is marked by a temporary increase of vertical velocity at 2 km and is followed by an increase of vertical velocity at middle and then upper levels. At the stage when maximum updraft strength is greatest, vertical velocity is maximized in the upper troposphere. Most of the time, the maximum vertical velocity occurs at midlevels, and vertical velocity is almost always greater at midlevels than at low levels immediately above the gust front.

In contrast, the time series from the center line region shows consistently weaker maximum vertical motions at midlevels than at low levels (Fig. 6b). In this time series there are three periods of enhanced 12 km vertical velocity that are associated with distinct updraft areas. The second maximum, present from roughly 168 to 198 min before slowly declining in strength over the next 20 min, is well defined and persistent. Superimposed on this updraft maximum is a higher-frequency and lower-amplitude variability that is associated with cells occurring within the relatively persistent ($t \sim 60$ min) updraft area. These cellular updraft perturbations, which are first apparent along the forward flank of the storm at low and then mid levels (e.g., C3, Fig. 7a), reach the upper troposphere and eventually become the dominant centers within the preexisiting updraft area (e.g., C3, Figs. 7e,f). The peaks within the broad 12-km updraft

---

[3] The size of the rectangles was optimally chosen to include entire middle- and upper-tropospheric updraft areas while minimizing the simultaneous sampling of additional separate updraft areas along the line.

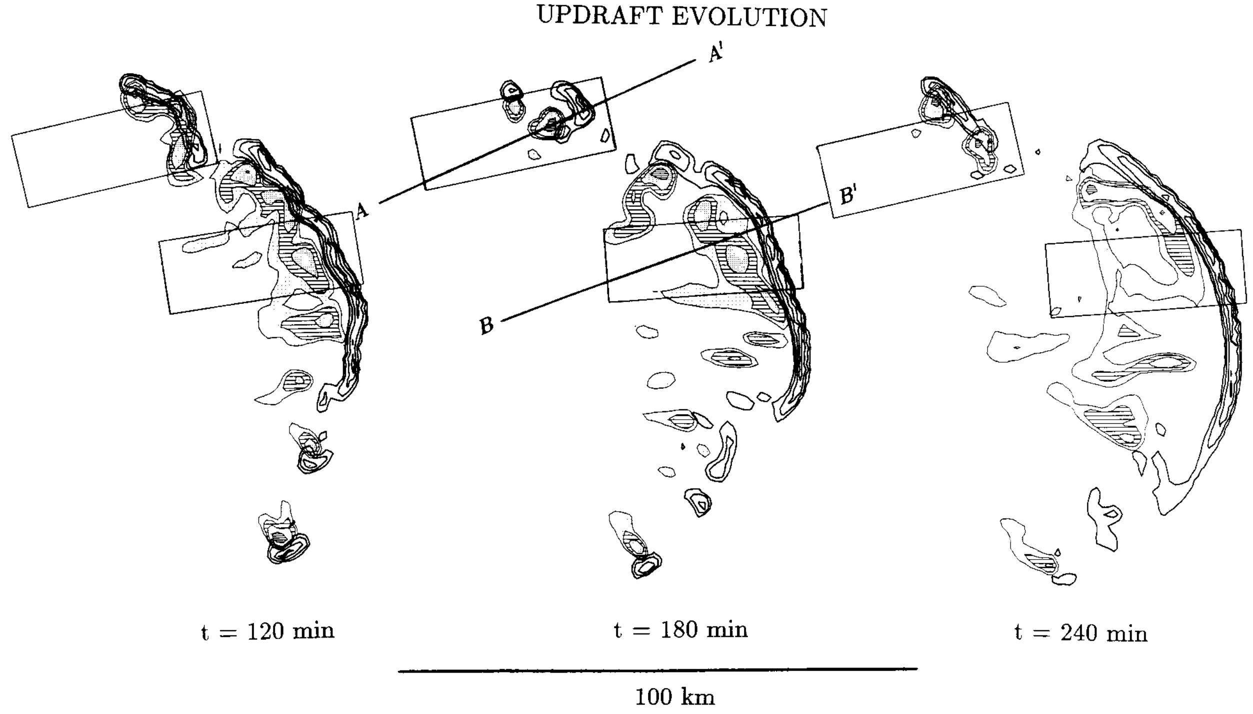

FIG. 5. Evolution of convective updrafts at 2 km MSL (1, 2.5, 5, and 7.5 $\mathrm{m\ s^{-1}}$ solid contour intervals) and at 6 km MSL with shading increments of 1–2.5 (dots), 2.5–5 (lines), 5–10 (dense dots), and $\geq$ 10 $\mathrm{m\ s^{-1}}$ (dense lines). *AA′* and *BB′* denote the location of the vertical cross sections displayed in Figs. 7 and 8, respectively. The rectangles indicate the horizontal domains for the time series displayed in Fig. 6.

maximum at 171, 183, and 195 min (Fig. 6b) are respectively associated with the development of the initial discrete cell C1 and the successive developments C2 and C3 along the forward flank of the updraft area (Figs. 7d–f). This process bears resemblance to the so-called weak evolution (Foote and Frank 1983) observed in stronger midlatitude storms. In two-dimensional numerical simulations in midlatitude environments, Fovell and Ogura (1989) found that the weak evolution mode where small perturbations occur within a generally continuous updraft zone is favored in environments of strong low-level vertical shear whereas the strongly evolving multicell that is characterized by development of distinct (separate) updraft centers is favored in weaker vertical shear.

Despite comparable low-level updraft strength, the upper-tropospheric maxima in the center line region are considerably weaker than their north flank counterparts (Fig. 6). Moreover, the individual middle- and upper-tropospheric maxima become successively weaker during the 2-h time series, a trend that is not evident along the north flank. This evolution is concurrent with the enhancement of the MCS-induced flow in the center line region (cf. Figs. 3c,d and 6b).

Structural differences between the north flank and center line regions suggested by the preceding time series are illustrated using cross sections that intersect the upper-tropospheric updraft areas close to their time of maximum strength. A vertical cross section from the north flank region (Fig. 8a) reveals a narrow convective updraft zone with a deep vertical velocity maximum in the middle and upper troposphere. The vertical structure in the center line region (Fig. 9a) consists of a deeper low-level updraft maximum near the leading edge, followed by a weaker and more strongly tilted convective zone at middle- and upper-tropospheric levels.

The center line cross section exhibits particularly weak upward motion in the middle troposphere. Although the time series (Fig. 6b) reveals that the midtropospheric minimum is a transient feature, along-line averages from this region obtained from both the simulation and observations (Trier et al. 1996, their Fig. 14) also exhibit a midtropospheric minimum situated between the leading-edge updraft maximum and an upper-tropospheric maximum 15–20 km rearward of the leading edge. The time series illustrates that midtropospheric minima in the vertical profile of $w_{\max}$ over the rectangular area occur when upper-tropospheric updraft centers are either near maximum strength or starting their decay (Fig. 6b). In both the observations and the simulation there are often multiple upper-tropospheric updraft areas that mature in close proximity to each other and thus may account for the line-averaged midtropospheric minimum. This updraft structure is particularly prominent during the earlier linear stage of the MCS and results in parallel bands of enhanced reflectivity in both the observations (Jorgensen et al. 1997) and the simulation. These bands are evident in the center

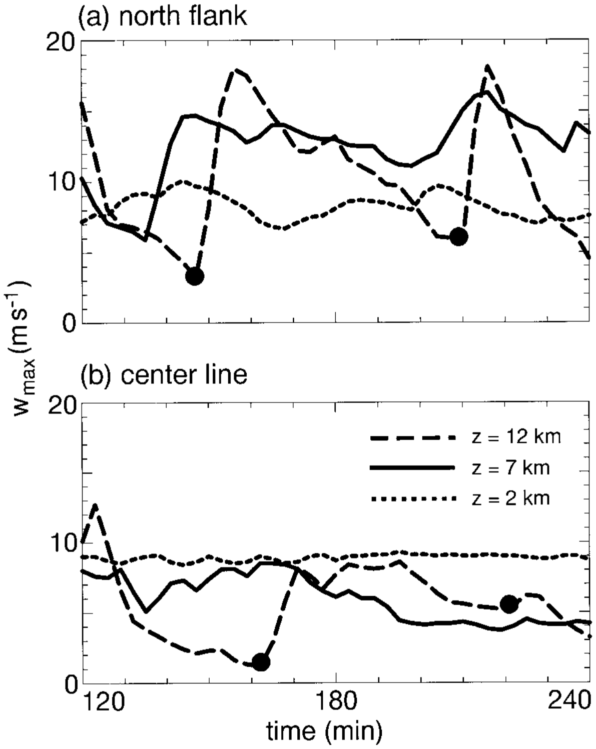

FIG. 6. Time series of maximum vertical velocity (m s^{-1}) at 2 (short dashed), 7 (solid), and 12 km MSL (long dashed) within the 15 km by 40 km rectangles depicted in Fig. 5 situated along (a) the north flank and (b) the central leading edge of the MCS. The solid circles superimposed on the 12-km time series indicate the occurrence of new (discrete) maxima that are not embedded within preexisting updraft areas at that level.

line region of the simulation at 2 h (Fig. 2). The most intense reflectivity is associated with the shallow leading-edge updraft and a second, weaker 10-km-wide band of enhanced reflectivity, located ~30 km to the rear, is associated with additional precipitation development in upper-tropospheric updrafts.

In addition to differences between convective updrafts, the degree of mesoscale structure in the low-level thermodynamic and flow fields varies from the north flank to the center line region. The low-level structure of the north flank cross section is similar to the density-current model of convective outflows (e.g., Charba 1974; Droegemeier and Wilhelmson 1987). In this region the low-level cold pool is strongest and deepest immediately rearward of the leading-edge updraft (Fig. 8b). A small-scale dynamic high is situated at the leading edge of the cold pool (Fig. 8d), where the flow is strongly convergent, and is followed by low dynamic pressure (Fig. 8d) associated with a weak rotor circulation behind the cold pool head (Fig. 8b). In the center line cross section there is a much more extensive (25-km scale) buoyancy-driven mesolow that extends from 1 to 5 km MSL, with stronger front-to-rear flow overlying an elevated and more areally extensive rear inflow (cf. Figs. 9c and 8c), and no evidence of a rotor circulation behind the dynamic high at the leading edge (Fig. 9d). The center line cross section also exhibits a mesoscale downdraft signature (Leary 1980) in the potential temperature field behind the leading convective zone (Fig. 9b), with a relatively cold region associated with evaporation and melting (z = 4–5 km) overlying a relatively warm subsidence zone (z = 1–4 km). A mesoscale downdraft signature is not present in the north flank cross section (Fig. 8b).

A third type of convective updraft structure is associated with the later development of the transverse precipitation bands near the southern end of the mature bow echo (Fig. 2). The evolution of midlevel system-relative flow (Fig. 10) shows that these reflectivity features become elongated as the front-to-rear flow intensifies and extends farther rearward with time behind the southern end of the leading-edge reflectivity maximum.

A vertical cross section (Fig. 11) through the transverse precipitation band exhibits some similarities to the center line cross section (Fig. 9). Here, however, the mesoscale pressure and flow features are stronger and more extensive (owing, in part, to a line-end vortex circulation) and, as we shall see in section 4b, exert an even greater influence on the updraft structure. The low-level flow that originates ahead of the MCS is lifted sharply through a shallow layer at the leading edge (Fig. 11a). This warm front-to-rear current (Fig. 11b) continues rearward and eventually feeds a series of weaker updrafts aloft (Fig. 11a) that give rise to the elongated precipitation bands.

b. Updraft trajectory analysis

In an effort to better understand the dynamics of convective updrafts, we analyze trajectories passing through updrafts occurring within the north flank, center line, and transverse band regions. The trajectories are calculated using the methodology employed in Weisman and Klemp (1984); here we use model output at 180-s intervals and an extrapolation interval of 100 m. We first present analysis of trajectories through simulated updrafts in the center line region, which is the location of the MCS that was best sampled by observations (Jorgensen et al. 1997). Results are then compared to trajectory calculations within simulated updrafts over the north flank and transverse band regions to elucidate the mechanisms influencing along-line variability.

Two basic trajectory types (Fig. 12) are identified with airflow through the the updraft area that contains the longer-lived upper-tropospheric maximum present from 168 to 198 min in the center line time series (Fig. 6b). Trajectory A passes through the center of upper-tropospheric (12 km MSL) updraft cell C2 (Fig. 7e) near its time of peak intensity. This trajectory originates near the surface (at 150 m MSL) to the east of the MCS. After strong ascent at the leading edge, it experiences a vertical deceleration in the middle troposphere and then experiences a secondary vertical acceleration in the

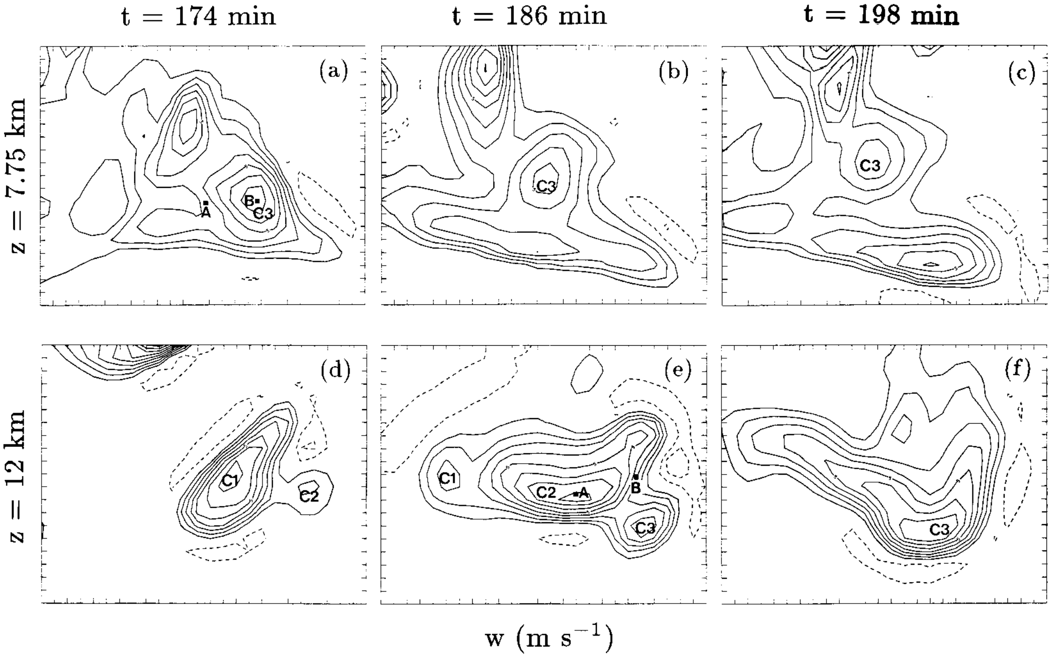

FIG. 7. Updraft structure over 25 × 20 km^2 model subdomains within the center line region from 174 to 198 min at (a)–(c) 7.75 km MSL and (d)–(f) 12 km MSL. Vertical motion is contoured in increments of 1 m s^{-1} (positive values solid, negative values dashed, and 0 m s^{-1} contour omitted). The dots associated with annotations A and B in (a) and (e), respectively, represent the location of trajectories A and B (Figs. 12 and 13) relative to the updraft structure in these cross sections. Trajectory B actually passes through the 12-km level ~ 10 s later than the time of the cross section in (e). The annotations C1, C2, and C3 identify individual updraft perturbations within the general updraft area.

upper troposphere (Figs. 12 and 13a). Trajectory B, on the other hand, passes through a middle tropospheric (7.75 km MSL) updraft maximum (Fig. 7a) associated with the development of the newer cell C3 along the forward flank of the general updraft area (Figs. 7e,f). This trajectory begins to ascend at 900 m MSL, above and to the northeast of trajectory A. Although the maximum height it attains is 1.2 km shallower, it is more steeply sloped than trajectory A through the older cell (Figs. 12 and 13a).

Both trajectories experience strong ascent within leading edge updraft cores above the gust front. However, in this region of strong system-relative flow (Fig. 9a), neither of the two trajectories remains within the center of individual updraft cells for the duration of trajectory ascent (cf. Figs. 7a,e). The relationship between updraft cells and trajectories contrasts with that found along the north flank (Fig. 8a), where trajectory paths through the center of updraft cells remain close to the location of the maximum updraft at any given level (not shown). Differences between the north flank and center line trajectories will be examined from a more detailed dynamical perspective shortly.

It is clear from the previous examples (trajectories A and B) that the weakening of vertical velocity along trajectories in the midtroposphere (Fig. 13a) can vary substantially depending on the location and age of the updraft cell that trajectories pass through. However, at least some weakening of vertical velocity above the low-level maximum updraft is a persistent characteristic of the center line time series (Fig. 6b) that is largely absent in the north flank time series (Fig. 6a).

The buoyancy along trajectories A and B (Fig. 13b) is partitioned into components associated with condensate loading (Fig. 13c) and virtual potential temperature perturbations (Fig. 13d). The lesser amount of condensate loading beneath 7 km along trajectory B is consistent with slightly stronger low-level vertical accelerations and a weaker midtropospheric vertical deceleration than those found along trajectory A (cf. Figs. 13a,c). However, larger thermal buoyancy along trajectory A (Fig. 13d), which results from this trajectory originating from a lower level (where θ_e is larger), offsets the additional condensate loading (Fig. 13b). Along both trajectories the condensate loading decreases during the midtropospheric vertical deceleration from ~5 to 7 km and remains relatively constant during the secondary vertical acceleration between 7 and 10 km. Thus, while the buoyancy along trajectories (Fig. 13b) is significantly reduced by condensate loading (Fig. 13c), consideration of the condensate loading alone cannot explain either the general shape of trajectory vertical motion profiles (i.e., the midtropospheric decelerations and upper-tropospheric accelerations) or the differences between these profiles. Moreover, the full buoyancy it-

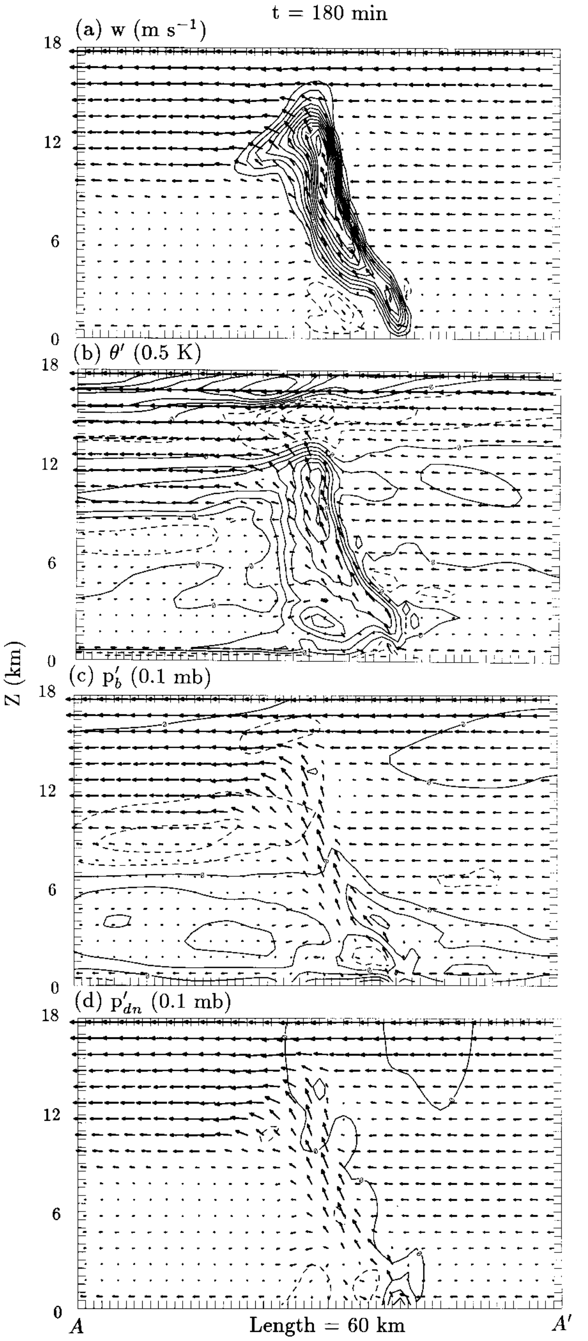

FIG. 8. Vertical cross section along *AA′* of Fig. 5 at 180 min illustrating the system-relative wind vectors in the plane of the cross section (a vector the length of a grid box is equivalent to 7.5 m s^{-1}) with (a) vertical motion (1 m s^{-1} contour intervals, negative values dashed and zero contour omitted), (b) temperature perturbation from the initial state (0.5-K contour intervals, negative values dashed), (c) buoyancy pressure perturbation (0.1-mb contour intervals, negative values dashed), and (d) dynamic pressure perturbation [contour intervals as in part (c)]. In all panels the vertical scale is exaggerated by a factor of 2.

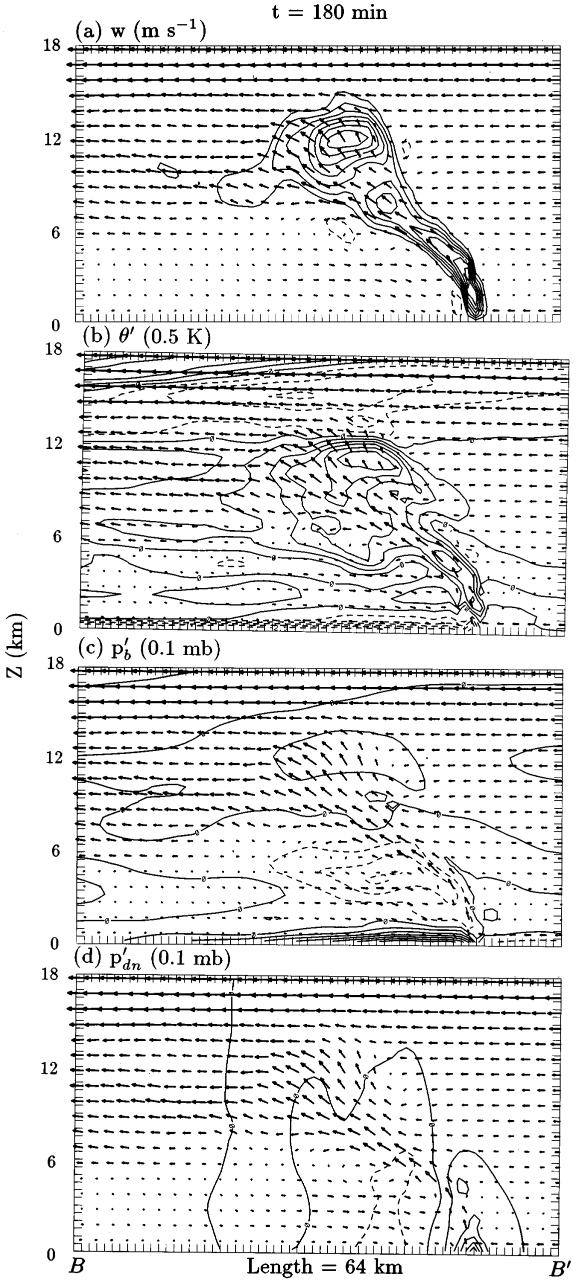

FIG. 9. As in Fig. 8 but along *BB′* of Fig. 5.

self is a poor indicator of the actual vertical accelerations experienced by these trajectories.

We now compare the forcing of vertical accelerations along trajectory A of Fig. 12 that passes through the upper-tropospheric updraft sampled in the center line cross section (Fig. 9a) with the forcing along back trajectories from mature updraft cells depicted in the north flank (Fig. 8a) and transverse band (Fig. 11a) cross sections. By comparing these trajectory calculations from updraft cores at similar stages of development, when these updraft centers situated above and rearward of the

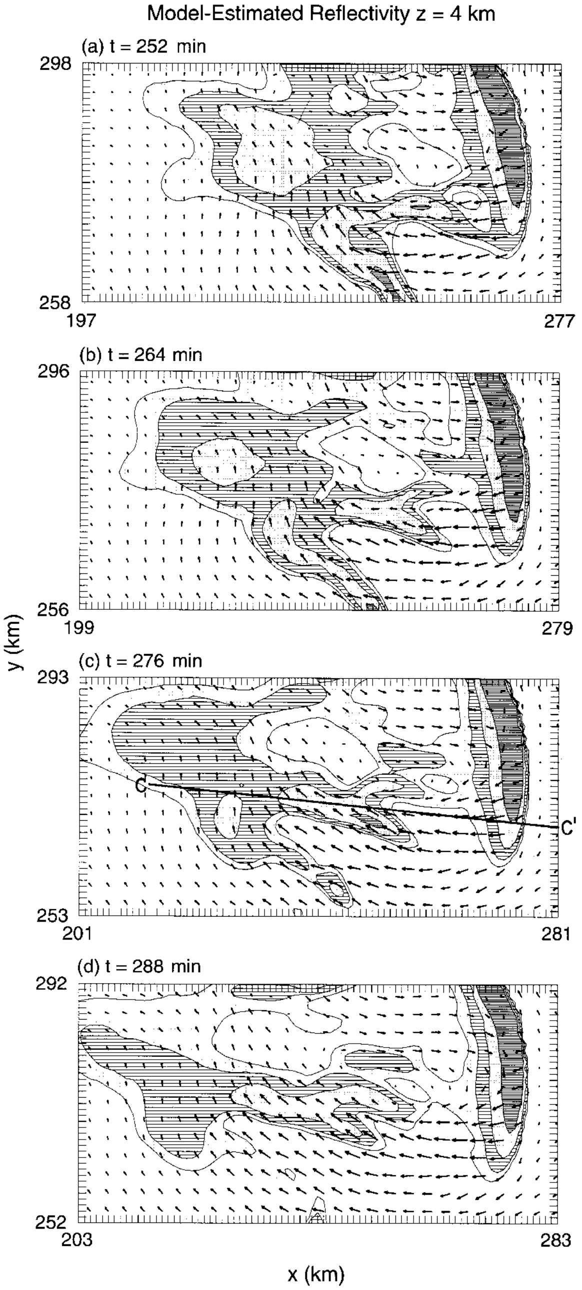

FIG. 10. System-relative horizontal winds (plotted as in Fig. 3) and model-estimated radar reflectivity (shading intervals as in Fig. 2) over a model subdomain that emphasizes evolution of an elongated precipitation band located rearward of and oriented transverse to the leading edge of the simulated MCS at (a) 252, (b) 264, (c) 276, and (d) 288 min. *CC*′ denotes the location of the vertical cross section displayed in Fig. 11.

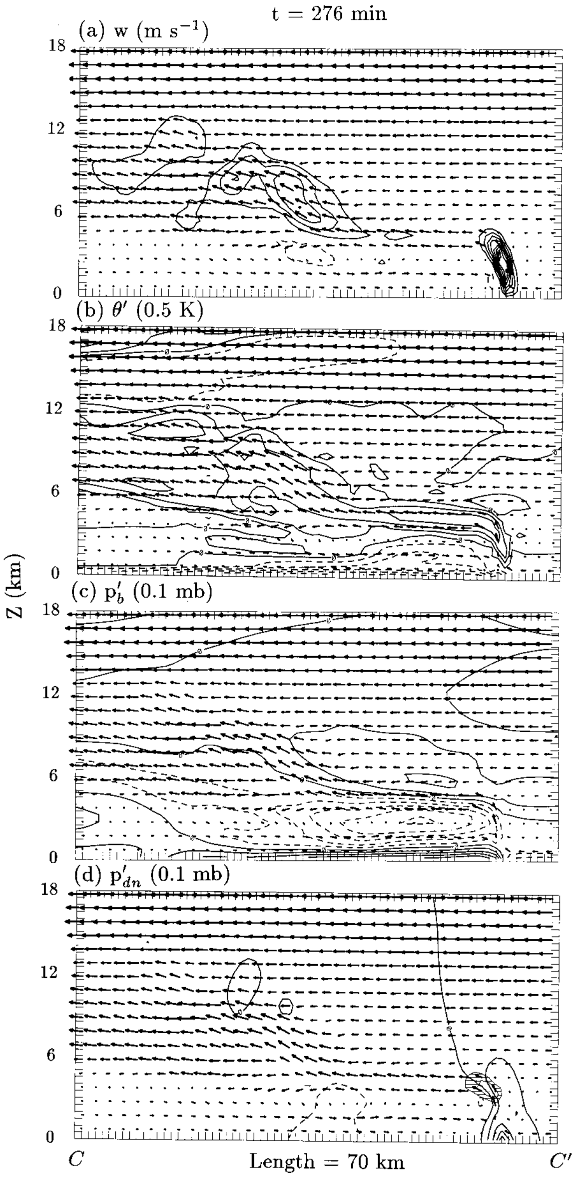

FIG. 11. As in Fig. 8 but along *CC*′ of Fig. 10c at 276 min. The shading in (d) represents the downward-directed vertical acceleration due to dynamic pressure (PZDN) of −0.005 to −0.015 m s^{-2} (lines) and ≤ −0.015 m s^{-2} (dots).

leading-edge updraft are at or near maximum strength, we can gain an understanding of mechanisms that account for the characteristically weak middle- and upper-tropospheric vertical velocity maxima of the center line time series (Fig. 6).

The forcing of vertical accelerations along updraft trajectories is determined using a form of the vertical momentum equation

$$\frac{Dw}{Dt} = -c_p\bar{\theta}_v\frac{\partial \pi_{\rm dn}}{\partial z} - \left(c_p\bar{\theta}_v\frac{\partial \pi_{\rm b}}{\partial z} - B\right) \qquad (4)$$

similar to forms used in previous studies of convective storm dynamics (e.g., Schlesinger 1984; Weisman and Klemp 1984; Chen 1991; Trier and Parsons 1995; McCaul and Weisman 1996). In this equation the first term on the right side (PZDN) represents the effect of dynamically induced vertical pressure gradients on vertical accelerations (DWDT). The second term on the

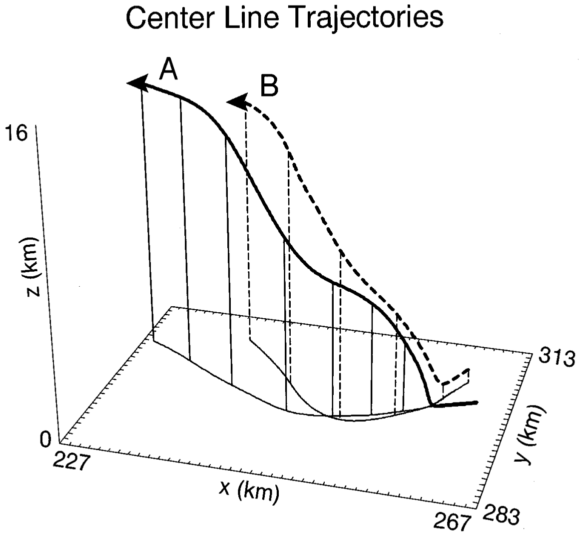

FIG. 12. Trajectory types associated with the airflow through the updraft center depicted in Fig. 7. Trajectory A (solid) is centered within the 12-km core of the older cell C2 at 186 min. Trajectory B (dashed) is centered at 7.75 km within the core of a midtropospheric updraft maximum at 174 min associated with the newer developing cell C3.

right side (enclosed by parentheses, PZBY) represents the net effect of buoyancy on vertical accelerations, which is a combination of the buoyancy B (BUOY) defined in (1) and the vertical pressure gradient force induced by the buoyancy pressure π_b. The effects of mixing, which are difficult to calculate directly, are neglected.

While trajectories emanating from updraft cores in all three regions originate at low levels ahead of the MCS (Fig. 14), air parcels decelerate vertically along portions of the trajectories through the center line and transverse band updrafts, whereas vertical acceleration occurs through the middle troposphere along the north flank trajectory (Fig. 15, top panel). The resulting strong upper-tropospheric vertical motion along the north flank trajectory occurs despite the fact that the buoyancy is considerably less than the buoyancy along the center line and transverse band trajectories (Fig. 15, bottom panel).

Along with the buoyancy, the forcing terms for vertical accelerations along the back trajectories from the three different regions are presented in the bottom panels of Fig. 15.[4] Both the transverse band trajectory A and the center line trajectory are characterized by a strong net downward acceleration that results from dynamic pressure (large negative PZDN), which occurs over a narrow zone immediately behind the leading edge updraft maximum from 268 to 273 min (cf. Figs. 14a and 15a) and from 163 to 170 min (cf. Figs. 14b and 15b), respectively. Subsequent upward vertical accelerations occur along both trajectories but are relatively weak (Figs. 15a,b), as only a small percentage of the buoyancy (BUOY) results in net buoyancy accelerations (PZBY).

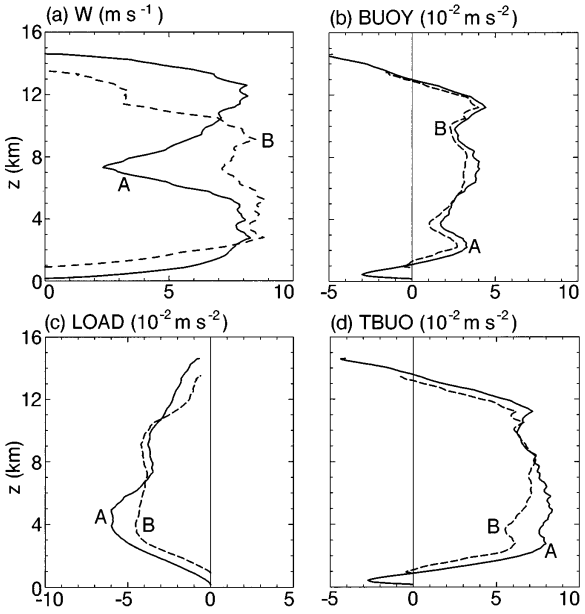

FIG. 13. Vertical profiles of (a) vertical velocity, (b) buoyancy (BUOY), (c) the contribution to buoyancy from condensate loading (LOAD), and (d) the contribution to buoyancy from virtual potential temperature perturbations from model initial state (TBUO) along the trajectories A (solid) and B (dashed) displayed in Fig. 12. For the time period in which values of these fields along the trajectories are plotted, trajectory height increases monotonically with time.

The inefficiency of midlevel buoyancy in leading to strong upward vertical accelerations in the center line and transverse band trajectories is associated with the presence of the extensive buoyancy-generated mesolow (Figs. 9c and 11c). The mesolow itself is linked in a reinforcing feedback process with the strong convectively generated mesoscale flow and is favored in these locations where the local orientation of the cold-pool edge of the incipient MCS relative to the environmental vertical shear favors rearward tilt (section 3). As pos-

---

[4] Vertical velocity derived from a backward integration of the forcing for vertical accelerations (DWDT = PZDN + PZBY) along transverse band trajectory (Fig. 15a, top panel) and the center line trajectory (Fig. 15b, top panel) is nearly identical to the actual vertical velocity in the middle and upper troposphere, which are the levels that differ most substantially between the center line and north flank time series (Fig. 6) and, accordingly, are of greatest interest. The discrepancy of w derived from the integrated forcing from actual values of w along the trajectories at the leading-edge updraft (Figs. 15a,b) results from the forcing terms overpredicting the net upward accelerations by nearly a factor of 2. This is true of all back trajectories examined from these two regions and likely results from the neglect of mixing in the integrated forcing, which is a compensating effect in the narrow low-level leading edge updraft cores that are adjacent to intense lateral gradients of w (Figs. 9a and 11a).

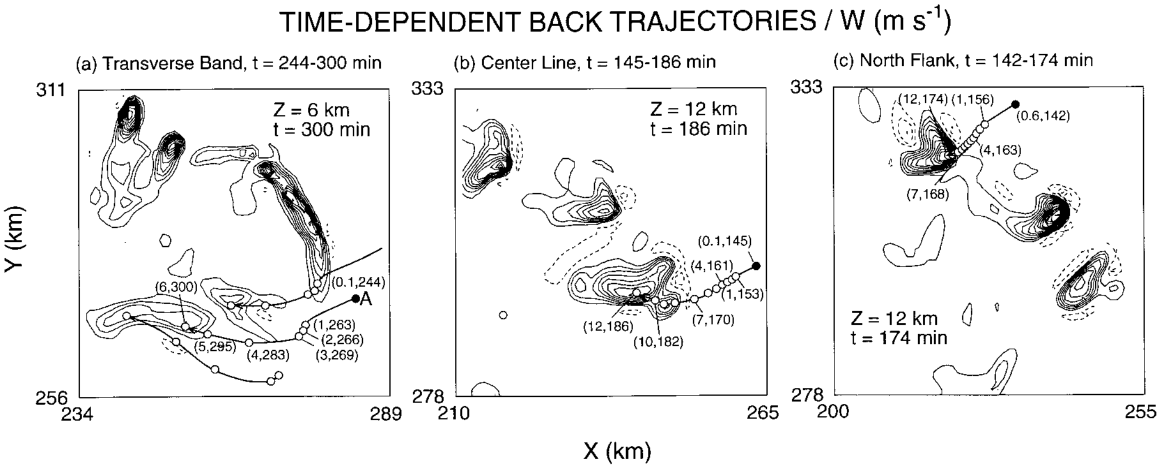

FIG. 14. Time-dependent back trajectories from (a) 6-km MSL updraft cores in the vicinity of the transverse precipitation bands starting at 300 min, (b) a 12-km MSL updraft core from the center line region starting at 186 min, and (c) a 12-km MSL updraft core from the north flank region starting at 174 min. The heights (km) and time of simulation (min) are annotated along the trajectory paths. Vertical motion at the starting time and height levels of trajectories are contoured in 1 m s^{-1} intervals (negative values dashed, zero contour omitted).

itively buoyant air parcels move rearward over the mesolow, their buoyancy is largely offset by the adverse vertical pressure gradient force associated with the buoyancy pressure [second term on the right side of (4)].

Along the north flank of the MCS, where deep convection is more isolated and a large buoyancy-induced mesolow does not occur (Fig. 8c), the midlevel buoyancy, although smaller than in the center line or transverse band updrafts, is more completely realized in the net buoyancy acceleration (Fig. 15c). Here, significant downward-directed contributions to vertical accelerations from dynamic pressure do not occur until there has already been substantial net buoyancy acceleration at midlevels (Fig. 15c). By contrast, downward-directed vertical accelerations due to dynamic pressure are associated with sharp minima in vertical motion in the midtroposphere behind the leading-edge updraft maxima along the center line and transverse band trajectories (Figs. 15a,b), where the MCS-induced front-to-rear flow is strong. As illustrated for the transverse band updraft, the strongest downward-directed dynamic pressure force (shaded in Fig. 11d) occurs where the flow begins to accelerate horizontally rearward in response to the

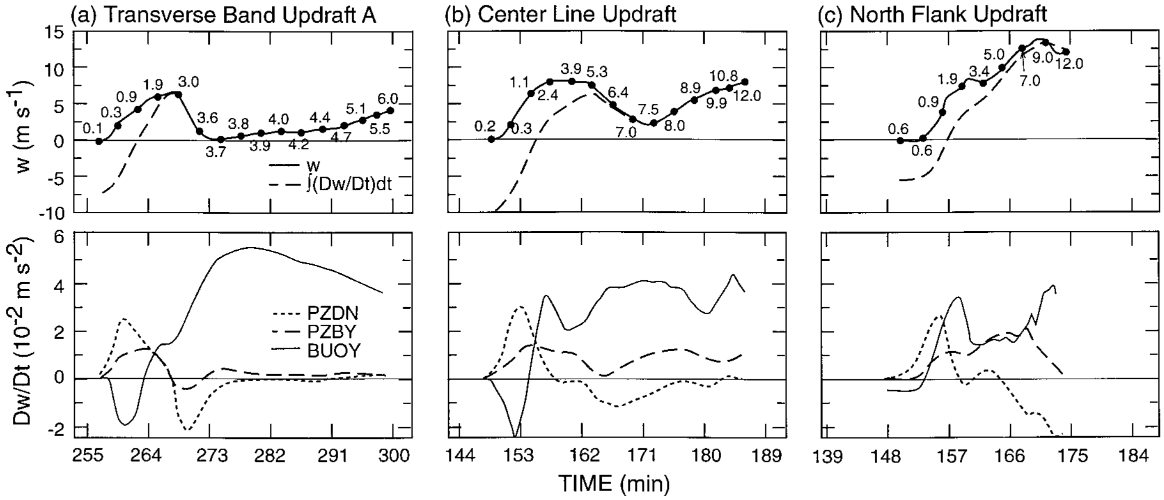

FIG. 15. Top panels: vertical velocity (solid) and vertical velocity calculated from a backward integration of the vertical acceleration forcing terms (DWDT = PZDN + PZBY) in (4) (dashed) along (a) the transverse band time-dependent back trajectory A of Fig. 14a; (b) the center line time-dependent back trajectory of Fig. 14b, which is a portion of trajectory A of Fig. 12; and (c) the north flank time-dependent back trajectory of Fig. 14c. The height (km) along the trajectories is annotated along the vertical velocity curve. Bottom panels: the vertical accelerations from the dynamic pressure (PZDN), net effect of buoyancy (PZBY), and buoyancy (BUOY) along the same trajectories for which vertical motions are plotted in the top panels.

buoyancy-generated mesolow (Fig. 11c) situated farther to the rear. Additional calculations (not presented) reveal that this downward-directed dynamic pressure force results almost entirely from the portion of the forcing on the right side of (2) that is associated with the interaction of the updraft and the MCS-induced vertical shear of the horizontal wind (i.e., $u'_z w_x - v'_z w_y$).

The close association of updraft structure with dynamically induced vertical pressure gradients has been reported in previous numerical studies of squall lines (e.g., Weisman et al. 1988; Chen 1991; Szeto and Cho 1994). The shallowness of the leading-edge updraft in the transverse band region of the current case may also be interpreted from a horizontal vorticity viewpoint (e.g., Rotunno et al. 1988; Weisman 1992, 1993). The negative horizontal vorticity associated with horizontal buoyancy gradients at the leading edge of the updraft may be nearly balanced by positive horizontal vorticity sources including the ambient low-level vertical shear and the MCS-induced vertical shear beneath the rear-inflow jet (Fig. 11a). Such a balance results in a condition favorable for strong low-level lifting at the gust front (e.g., Weisman 1992). However, the midlevel negative horizontal vorticity associated with the strong MCS-induced vertical shear, between the rear-inflow jet and the strong front-to-rear flow above, is unbalanced and thus not optimal for deep lifting. As a result, the lifting at the leading edge is strong but relatively shallow.

5. Vortex circulations

As noted in section 3, the transition of the central convective band to a bow morphology is concurrent with development of mesoscale vortices at its ends. While these vortex circulations are secondary to the interaction of the spreading storm-induced cold pool with the ambient low-level vertical shear as a mechanism governing general MCS growth, they are important since they impact the overall internal mesoscale flow structure of the MCS.

a. Structure of the line-end vortices

Vertical vorticity, $\zeta\mathbf{k} = (v_x - u_y)\mathbf{k}$, does not exist in the horizontally homogeneous base state of the simulations. However, it may be produced through the tilting of horizontal vorticity, $\boldsymbol{\omega}_h = (w_y - v_z)\mathbf{i} + (u_z - w_x)\mathbf{j}$. By 2 h, vortex development has begun near breaks in the leading edge updraft pattern where horizontal gradients of vertical motion exist (Fig. 16a). Although maximum vertical vorticity values decrease somewhat, the scale of the vortex circulations increases substantially during the following 2 h (Fig. 16b). The counterclockwise circulation of the northern vortex is more intense. A strong counterclockwise circulation forms in the vicinity of a break in the northern portion of the line in the observations (Jorgensen et al. 1997) and is similar in scale and strength to the simulated northern vortex (Trier et al. 1996, their Fig. 5). There is enhanced front-to-rear flow at midlevels and some evidence of a clockwise vortex circulation near the southern end of the leading edge of enhanced reflectivity in the observations, but this circulation is not nearly as well defined as the southern clockwise circulation in the simulation. Reasons for these differences between the observations and simulation are unclear.

Vertical cross sections illustrate major structural differences between the simulated northern and southern vortices. A north–south-oriented vertical cross section (Fig. 17a), which intersects the northern line end and vortex center, shows a vertically erect mesoscale center of enhanced vertical vorticity extending from 0.5 to 5.5 km. Its position beneath and rearward of a sloping convective updraft suggests that vortex stretching, $\zeta w_z > 0$, is a significant vorticity generation mechanism. This will be confirmed by trajectory analysis in section 5b.

The vortex center is located above the cold-pool negative buoyancy and below a region of positive buoyancy aloft associated with a weaker mesoscale updraft (Fig. 17a) situated rearward of the sloping convective updraft. The presence of the persistent mesoscale updraft above the vortex core suggests the potential role of vortex stretching on larger scales in sustaining the vortex, as has been discussed in numerous observational studies (e.g., Verlinde and Cotton 1990; Johnson and Bartels 1992; Brandes and Zeigler 1993; Keenan and Rutledge 1993; Jorgensen and Smull 1993; Scott and Rutledge 1995) of larger MCVs that occur primarily within the stratiform precipitation region of mature-to-decaying MCSs. The vertically erect structure of the northern vortex is maintained from 3.5 to 5 h, and some additional growth in depth (from 5.5 to 6.5 km) and east–west extent (from 15 to 25 km) of the region of enhanced vertical vorticity ($\zeta > 0.001\ \mathrm{s}^{-1}$) occurs during the period from 4 to 4.5 h as the fully developed bow-echo structure is attained (not shown).

In sharp contrast to the deep and vertically coherent northern vortex (Fig. 17a), the clockwise southern vortex center (Fig. 17b, dashed contours) is weaker, tilts toward the north, and is less than 2 km deep at any given location. Since horizontal gradients of vertical motion allow vertical vorticity generation through the tilting mechanism at the *w*-line ends, the strong south-to-north vertical slope of the southern vortex may be a consequence of the similar slope of the southern *w*-line end (Fig. 18). Due to this horizontal variability, significant tilting at any given horizontal location would occur only through a shallow depth. There is far less horizontal variability with height of the location of the northern line end in the vicinity of the much deeper and more erect northern vortex (Fig. 18). Since the northern vortex is most consistent with observations, it will be the focus of our analysis in the remainder of this section.

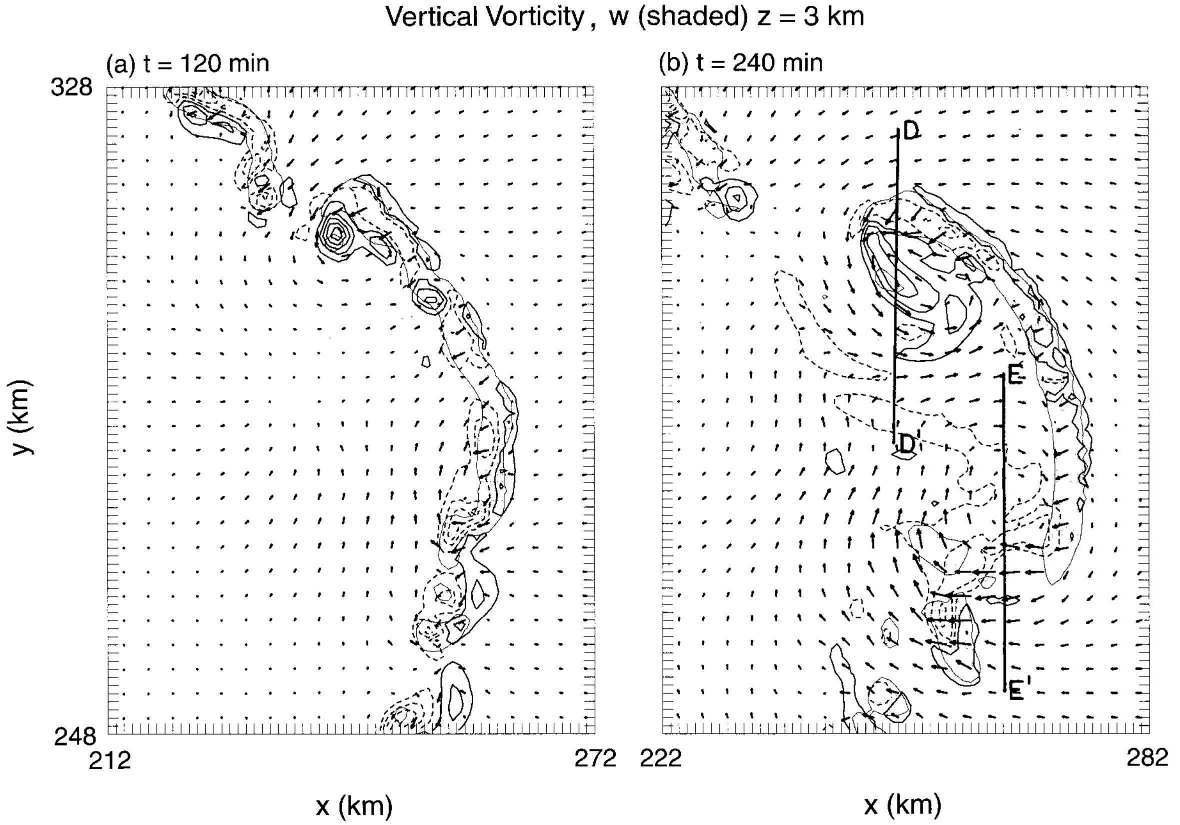

FIG. 16. The 3-km MSL system-relative wind vectors with vertical vorticity contoured in increments of 0.002 s^{-1} [positive values (counterclockwise rotation) solid, starting at 0.001 s^{-1}; negative values (clockwise rotation) dashed, starting at -0.001 s^{-1}] within a 60 × 80 km^2 model subdomain at (a) 120 and (b) 240 min. Vectors are plotted every third model grid point, with a vector length of one grid box equivalent to 5 m s^{-1}. In each panel, shading represents the 3-km MSL updraft $\geq$ 1 m s^{-1}.

b. Trajectory analysis of the northern vortex

The sources of vertical vorticity for the northern vortex are most easily illustrated by analysis of key groups of trajectories that pass through the vortex. Over 100 time-dependent 1-h backward trajectories from the region of large vertical vorticity ($\zeta \geq 0.0025$ s^{-1}) at 240 min (growth stage of the vortex) are calculated to determine the origin of vortex air parcels at the 1.5-, 3-, and 4.5-km levels. The vertical vorticity equation

$$\frac{D\zeta}{Dt} = -\zeta(\nabla\cdot\mathbf{v}_h) + \boldsymbol{\omega}_h\cdot\nabla w \qquad (5)$$

is then used to determine the vertical vorticity generation mechanisms along these trajectories. In (5), the term on the left side represents the time rate of change of vertical vorticity, while the first and second terms on the right side represent the generation of vertical vorticity from horizontal convergence of vertical vorticity (stretching) and differential vertical motion interacting with horizontal vorticity (tilting), respectively. The generation of vertical vorticity due to horizontal pressure–density solenoids is considerably smaller (Skamarock et al. 1994) and is neglected. The effect of mixing on vertical vorticity along trajectories is also neglected, although we shall return to this point. Trajectories are calculated in the same manner as those through the convective updrafts discussed earlier, but with 80-s temporal resolution.

Examples of the principal 1-h backward trajectories emanating from the western and central/east regions of the vortex at the 1.5- and 3-km levels are shown in Fig. 19. The trajectories from the 4.5-km level do not include any significantly different airstreams and are not discussed. The trajectories from the western flank (Figs. 19a,b) are the most recent to move through the primary vertical vorticity source region (denoted by the dashed part of trajectories in Fig. 19), which is along the southern portion of the line-end convective updraft.

There are two fundamental trajectory paths. One type (e.g., trajectory A in Fig. 19b) originates from within the boundary layer northeast and ahead of the MCS and moves southward underneath the core of the low-level convective updraft. It gains vertical vorticity while rising and moving southward at the southwestern (back) edge of this rearward tilting updraft (cf. Fig. 17a). The second type (e.g., trajectory B in Fig. 19b) originates behind the convective region at a height well above the pre-MCS boundary layer. This "rear-inflow" trajectory

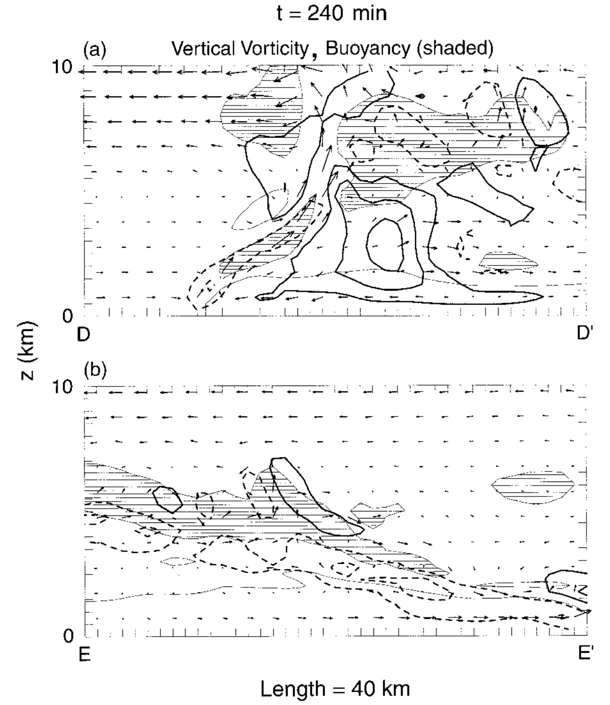

FIG. 17. System-relative wind vectors in the direction parallel to vertical cross sections along (a) *DD′* and (b) *EE′* of Fig. 16 at 240 min. In both panels vertical vorticity is contoured in increments of 0.002 s^{-1} (positive values solid, starting at 0.001 s^{-1}; negative values dashed, starting at -0.001 s^{-1}); buoyancy values ≥ 0.02 m s^{-2} (lines) and ≤ -0.02 m s^{-2} (dots) are shaded. The system-relative flow vectors within the cross section are plotted as in Fig. 8. In both panels the vertical scale is exaggerated by a factor of 2.

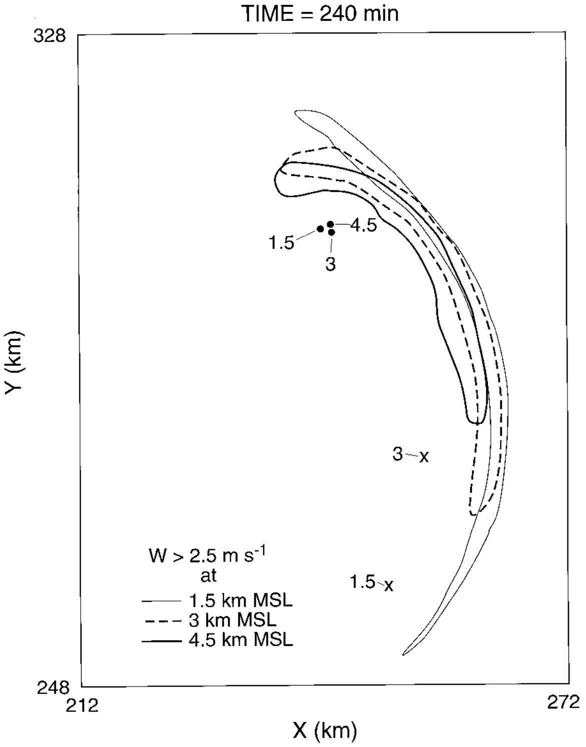

FIG. 18. Vertical motion along the leading-edge updraft at 240 min in excess of 2.5 m s^{-1} at 1.5 (thin solid contour), 3 (dashed contour), and 4.5 km MSL (bold solid contour). Dots (×'s) indicate the location of the northern (southern) circulation center at 1.5, 3, and 4.5 km MSL. There is no well-defined closed southern circulation center at 4.5 km MSL at 240 min.

slowly descends as it moves eastward and then northward toward the convective region of the MCS. It subsequently rises (more gradually than trajectory A) while acquiring significant vertical vorticity along the southern (back) edge of the leading convective updraft, and then loses a small amount of vertical vorticity in a weak downdraft after it turns southward toward the vortex core. Nearly all back trajectories from all three levels acquire the bulk of their vertical vorticity near the convective line-end region. The one exception is a class of back trajectories that emanate from the eastern flank of the vortex, a significant distance from the maximum vertical vorticity. These trajectories, exemplified by trajectory C in Fig. 19c, acquire vertical vorticity at a considerably more modest rate in the low-level rear inflow current a substantial distance from the leading edge of the squall line.

While the presquall boundary layer (A) and rear-inflow (B) trajectories both acquire their vertical vorticity within the convective zone of the MCS, the details by which vertical vorticity generation occurs along these two types of trajectories are somewhat different. In the region of significant vertical vorticity increase (indicated by dashed lines in Fig. 19), trajectory A (Fig. 20a) initially has substantial negative vertical vorticity and undergoes strong positive tilting during a 6-min period as it rises to ~2 km in the low-level updraft. After the vertical vorticity exceeds zero, stretching begins to contribute to and eventually dominates vertical vorticity generation as the trajectory continues to rise. The positive influence of stretching lasts longer than tilting (Fig. 20a), but its contribution to vertical vorticity generation is comparable (Fig. 20b). Along trajectory B (Fig. 21a), the initial positive tilting is much weaker but lasts considerably longer than along trajectory A. As for trajectory A, stretching becomes more important as vertical vorticity increases. In contrast to trajectory A, the integrated tilting over the period of vertical vorticity increase decreases and eventually becomes weakly negative (cf. Figs. 20b and 21b). However, tilting is still important since it produces the initial vertical vorticity that is subsequently strongly stretched (Fig. 21a).

For these two trajectories and for a large majority of the additional trajectories calculated backward from near the vortex core region, the sum of the integrated tilting and stretching forcing terms results in an overestimate of the actual vertical vorticity increase during the 20–25-min generation period by 10%–40%. For trajectories A and B, the overestimates are 14% (Fig. 20b)

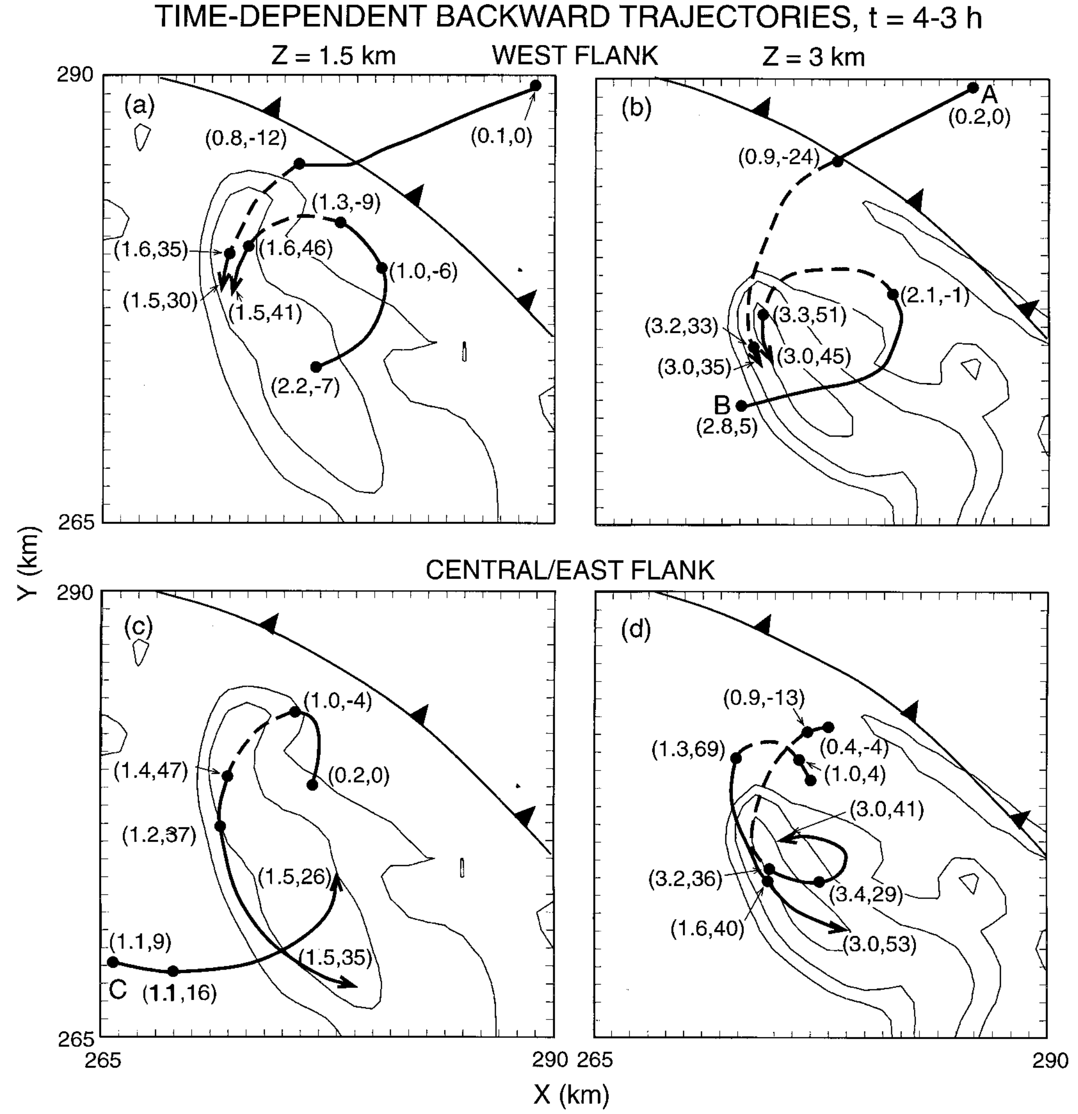

FIG. 19. Representative time-dependent back trajectories from 240 to 180 min originating from (a) the west flank of the northern vortex at 1.5 km MSL, (b) the west flank of the northern vortex at 3 km MSL, (c) the central/east flank of the northern vortex at 1.5 km MSL, and (d) the central/east flank of the northern vortex at 3 km MSL. Heights in kilometers (left) and vertical vorticity in units of 10^{-4} s^{-1} (right) are annotated at selected locations along trajectories. Regions of substantial vertical vorticity gain ($D\zeta/Dt \geq 10^{-6}$ s^{-2} over periods of 5 min or more) along trajectories are denoted by the dashed portions of the trajectory curves. Vertical vorticity values at the trajectory origination levels are contoured (thin lines) at thresholds of ζ = 0.001, 0.0025, and 0.005 s^{-1}. The position of the surface gust front, as approximated by the −0.5-K potential temperature perturbation contour, is indicated by the solid barbed symbol. Note that the annotated trajectories A and B are not related to the updraft trajectories A and B of Fig. 12.

and 29% (Fig. 21b), respectively. Discrepancies of this order may be explained by dissipation from mixing near regions of strong horizontal gradients of vertical vorticity along the trajectories.

c. Horizontal vorticity source for the northern vortex

For the presquall trajectory, the tilting of the ambient vertical shear contributes only slightly to positive vertical vorticity generation at the onset of the vertical vorticity increase (Fig. 20a). For the rear-inflow trajectory, tilting of the ambient vertical shear is negative during the entire vertical vorticity increase (Fig. 21a). Since either none or very little of the vertical vorticity generation from tilting is directly associated with the ambient vertical shear, it must result from tilting of the vertical shear (horizontal vorticity) associated with the MCS-induced flow.

In the absence of mixing, the horizontal vorticity equation

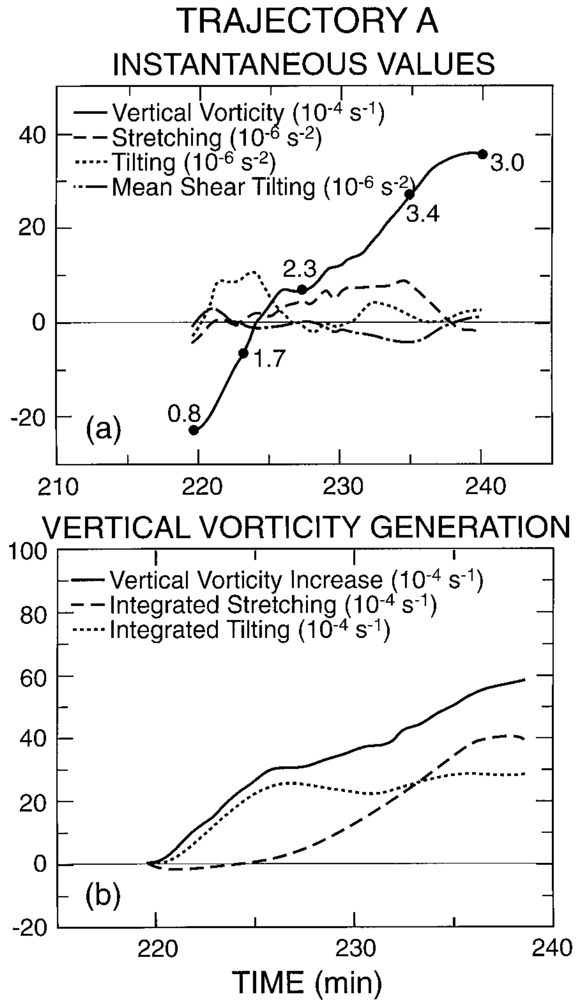

FIG. 20. (a) Instantaneous values of vertical vorticity (10^{-4} s^{-1}, solid line), stretching (10^{-6} s^{-2}, dashed line), total tilting (10^{-6} s^{-2}, dotted line), and tilting of ambient shear (10^{-6} s^{-2}, dash–dotted line) from the approximate beginning of significant vertical vorticity increase along trajectory A (position indicated by the beginning of the dashed line in Fig. 19b) to the origination point of the back trajectory at 3 km MSL. The height (km) of the trajectory is annotated along the vertical vorticity curve. (b) Vertical vorticity increase (10^{-4} s^{-1}, solid line), integrated stretching (10^{-4} s^{-1}, dashed line), and integrated total tilting (10^{-4} s^{-1}, dotted line) during the period of vertical vorticity increase along trajectory A. Note that the time scales on the horizontal axes of (a) and (b) are not identical.

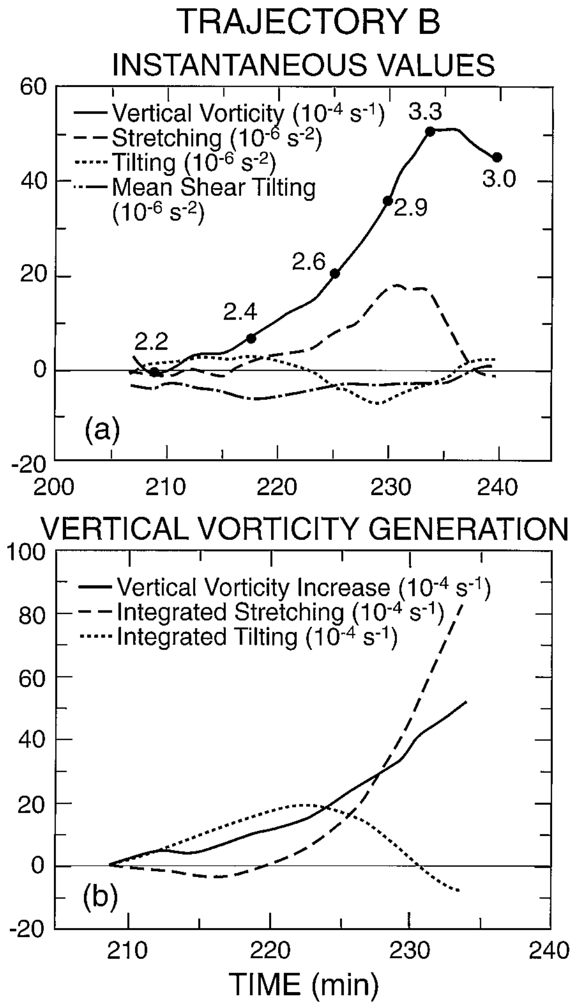

FIG. 21. As in Fig. 20 but for trajectory B of Fig. 19b.

$$\frac{D\boldsymbol{\omega}_h}{Dt} = \boldsymbol{\omega}\cdot\nabla\mathbf{v}_h + \nabla \times (B\mathbf{k}) \qquad (6)$$

indicates that horizontal vorticity changes along trajectories may arise from a combination of tilting of vertical vorticity and convergence (stretching) of horizontal vorticity [first term on the right side of (6)] and generation due to horizontal buoyancy gradients [second term on the right side of (6)]. Along the rear-inflow trajectory path, denoted by the triangle symbols in Fig. 22, horizontal vorticity increases approximately an order of magnitude from 0.0018 to 0.0103 s^{-1} as the path enters and subsequently moves northwestward within the buoyancy gradient at the back edge of the convective updraft. From (6), the orientation of the horizontal vorticity nearly perpendicular to the buoyancy gradient in the vicinity of the trajectory path (Figs. 22b–d) implies buoyant production of horizontal vorticity.

The dots in Fig. 23 locate the position of maximum tilting of horizontal to vertical vorticity, relative to the vertical motion and horizontal vorticity fields, for both the presquall (Fig. 23a) and rear-inflow (Fig. 23b) trajectories. Trajectories that originate from ahead of the MCS spend a shorter time within the buoyancy gradient rearward of the maximum updraft than do the rear-inflow trajectories. However, these presquall trajectories pass closer to the line end, where a more substantial portion of the horizontal gradient of vertical motion is parallel to the horizontal vorticity (Fig. 23a). These differences explain why vertical vorticity generation from tilting in the presquall trajectories is more intense, but of shorter duration, than that found along the rear-inflow trajectories (cf. Figs. 20a and 21a).

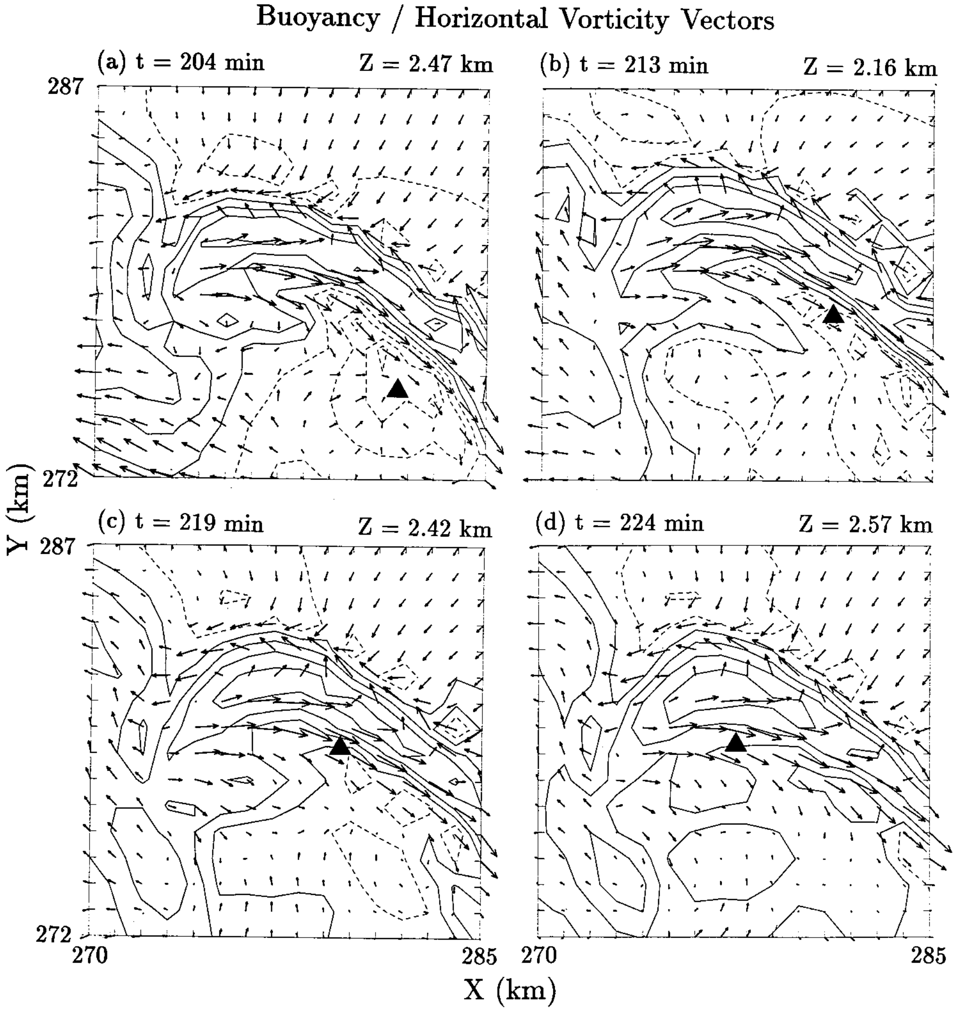

FIG. 22. Buoyancy contoured in intervals of 0.01 m s^{-2} (positive values solid, starting at 0.005 m s^{-2}; negative values dashed, starting at -0.005 m s^{-2}) with horizontal vorticity vectors superimposed (a vector length of one grid box is equivalent to 0.01 s^{-1}) at (a) $z = 2.47$ km and $t = 204$ min, (b) $z = 2.16$ km and $t = 213$ min, (c) $z = 2.42$ km and $t = 219$ min, and (d) $z = 2.57$ km and $t = 224$ min. The centroid of triangles on each panel indicates the position of trajectory B from Figs. 19b and 21.

The importance of tilting associated with buoyantly produced (MCS-induced) vertical shear has also been suggested and illustrated schematically for the early stages of vortex generation within larger midlatitude MCVs (Davis and Weisman 1994b). The relatively small direct importance of the horizontal vorticity associated with the ambient vertical shear in the generation of vertical vorticity contrasts with smaller-scale midlevel mesovortex development in supercell thunderstorms (e.g., Rotunno and Klemp 1982; Davies-Jones 1984) and line-end vortices within midlatitude bow echoes (Weisman 1993) that develop in environments of larger CAPE and stronger vertical wind shear.

6. Summary and discussion

In this study we examine the three-dimensional structure and evolution of a numerically simulated tropical squall line. The simulation accurately captures the transition of a portion of the leading edge of the observed squall line from a quasi-linear morphology oriented approximately perpendicular to a low-level jet to a highly three-dimensional bow echo (Trier et al. 1996). Many aspects of the mesoscale evolution (section 3) resemble simulations of more intense midlatitude bow echoes (Weisman 1993) that occur in environments of larger CAPE and stronger vertical wind shear. In the current study, we analyze well-simulated structural characteristics reported in Trier et al. (1996), including the convective updraft structure and its variability along the leading edge of the MCS (sections 4a,b), the development of a mesoscale vortex during the transition to the bow-echo stage (sections 5b,c), and the elongated transverse precipitation bands that occur during the fully developed bow-echo stage (sections 4a,b).

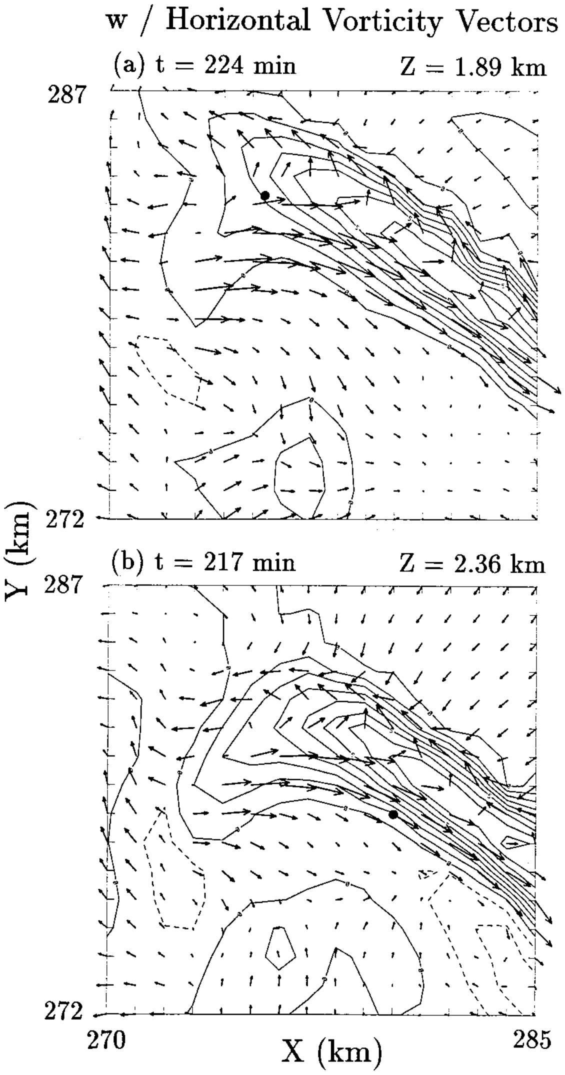

FIG. 23. Vertical motion contoured in intervals of 1 m s^{-1} (negative values dashed) with horizontal vorticity vectors superimposed (vectors are scaled as in Fig. 22) at the height and time of maximum tilting along (a) trajectory A of Figs. 19b and 20, and (b) trajectory B of Figs. 19b and 21. The position of maximum tilting along trajectory A (B) is indicated by the dot in (a)[(b)].

Systematic variations of convective updraft strength and vertical structure between the central and northern portions of the MCS are quantified using regional time series of maximum vertical velocity at different levels. In both the observations (Jorgensen et al. 1997) and this simulation, a common (but not persistent) vertical structure along the central portion of the MCS consists of a shallow leading-edge updraft maximum, followed by a midtropospheric minimum ahead of an upper-tropospheric updraft maximum. The time series from this region suggests that this structure occurs when evolving updraft cells in the upper troposphere are near maximum strength or starting their decay. In contrast, for the stronger, more isolated convection along the northern flank of the simulated MCS, maximum vertical velocity is almost always stronger at midlevels than at low levels.

Trajectory analysis is used to investigate mechanisms influencing the systematic variability in updraft strength and organization. The relatively weak middle- and upper-tropospheric vertical velocities in deep convection near the central portion of the MCS are associated with downward-directed dynamic pressure forces that occur above and immediately rearward of the persistent leading-edge updraft maximum and a near balance between buoyancy and the vertical pressure gradient force associated with the buoyancy-induced pressure farther to the rear. The downward-directed dynamic pressure forces are most intense along portions of the leading edge where the MCS-induced horizontal flow and its associated vertical shear are particularly strong. Only after air parcels move rearward, and slowly upward and away from the strong downward-directed dynamic pressure force, are upward vertical accelerations due to buoyancy realized. However, these vertical accelerations that occur well rearward of the leading edge are relatively weak and are consistent with the presence of an MCS-induced circulation that has spread the positive buoyancy rearward over a broad area, which results in a low-to-midlevel mesolow and an associated buoyancy-induced vertical pressure gradient that significantly counteracts the vertical acceleration from buoyancy itself. The particularly weak secondary vertical accelerations and strong rearward horizontal accelerations that result in the elongated character of the transverse precipitation bands, situated rearward of the leading edge of the MCS during the later bow-echo stage, represent an extreme manifestation of this effect.

The strong MCS-induced horizontal flow and mesoscale zone of midlevel buoyancy are themselves initiated by factors that promote the initial rearward tilt of the convective updraft zone. These factors include the strength of the arc-shaped cold pool during the early stages of MCS development and the local alignment of its leading edge perpendicular to a significant component of the environmental reverse vertical shear above the low-level jet. Where the cold pool of the incipient MCS is weak and its leading edge parallel to this environmental vertical shear (e.g., the north flank of the MCS), deep convection remains more isolated and displays less rearward tilt. There the resulting small horizontal scale of the buoyancy (relative to that of the central portion of the MCS) is more efficient in promoting midtropospheric vertical accelerations.

The MCS-induced horizontal flow and its associated vertical shear, in addition to influencing updraft structure along the leading edge of the MCS, strongly affects the development of the simulated northern line-end vortex. This vertical shear, which arises from MCS-induced horizontal buoyancy gradients at the back edge of the sloping updraft, is a major horizontal vorticity source for air parcels that subsequently constitute the mesoscale vortex core. The vortex air trajectories are found to be of two primary types, including one type that originates within the boundary layer ahead of the MCS and another that originates rearward of the convective zone well above the boundary layer. Both trajectory types experience horizontal vorticity generation upon entering the horizontal buoyancy gradient, and vertical vorticity generation occurs as the horizontal vorticity is tilted and subsequently stretched along these air trajectories.

Asymmetries in squall-type MCSs can result from a variety of mechanisms. For instance, the importance of Coriolis forces in the three-dimensional evolution of midlatitude MCSs is widely recognized (e.g., Skamarock et al. 1994). In the current study we have added to previous numerical modeling work by illustrating how an ambient wind profile, in which the vertical shear varies with height in both magnitude and direction, can support strong asymmetries in a near-equatorial squall-type MCS. The systematic meso- and convective-scale variations that occur during the mature stage of the simulated MCS arise in the absence of horizontal gradients in the storm environment. This suggests that the overall representativeness of two-dimensional simulations of squall line convection in strong vertical shear needs to be carefully considered for cases in which there is an absence of strong and persistent external linear forcing. A remaining topic to be investigated concerns the extent to which changes in MCS organization during its life cycle (e.g., development of mesoscale vortices, changes in updraft structure) affect the large-scale heat and momentum budgets.

Acknowledgments. The authors have benefited from discussions concerning this work with Scott Braun (NCAR), David Jorgensen and Bradley Smull (NOAA/NSSL/MRAD), Richard Johnson (Colorado State University), and Louis Wicker (Texas A&M University), and from constructive internal reviews of the manuscript by Chris Davis (NCAR), Richard Rotunno (NCAR), and Richard Carbone (NCAR). Robert Fovell (UCLA) and two anonymous reviewers provided criticisms and suggestions that helped to clarify aspects of this manuscript. This work was sponsored by the National Science Foundation (Grant 9215507).

REFERENCES

Barnes, G. M., and K. Sieckman, 1984: The environment of fast- and slow-moving tropical mesoscale convective cloud lines. *Mon. Wea. Rev.,* **112,** 1782–1794.

Brandes, E. A., and C. L. Ziegler, 1993: Mesoscale downdraft influences on vertical vorticity in a mature mesoscale convective system. *Mon. Wea. Rev.,* **121,** 1337–1353.

Charba, J., 1974: Application of gravity-current model to analysis of squall-line gust front. *Mon. Wea. Rev.,* **102,** 140–156.

Chen, C.-S., 1991: A numerical study of a squall line over the Taiwan Strait during TAMEX IOP 2. *Mon. Wea. Rev.,* **119,** 2677–2698.

Chong, M., P. Amayenc, G. Scialom, and J. Testud, 1987: A tropical squall line observed during the COPT 81 experiment in West Africa. Part 1: Kinematic structure inferred from dual-Doppler radar data. *Mon. Wea. Rev.,* **115,** 670–694.

Davies-Jones, R. P., 1984: Streamwise vorticity: The origin of updraft rotation in supercell storms. *J. Atmos. Sci.,* **41,** 2991–3006.

Davis, C. A., and M. L. Weisman, 1994a: Balanced dynamics of mesoscale vortices produced in simulated convective systems. *J. Atmos. Sci.,* **51,** 2005–2030.

——, and ——, 1994b: Balanced dynamics of mesoscale vortices produced in simulated convective systems. Preprints, *Sixth Conf. on Mesoscale Processes,* Portland, OR, Amer. Meteor. Soc., 538–541.

Droegemeier, K. K., and R. B. Wilhelmson, 1987: Numerical simulation of thunderstorm outflow dynamics. Part I: Outflow sensitivity and turbulence dynamics. *J. Atmos. Sci.,* **44,** 1180–1210.

Foote, G. B., and H. W. Frank, 1983: Case study of a hailstorm in Colorado. Part III: Airflow from triple-Doppler measurements. *J. Atmos. Sci.,* **40,** 686–707.

Fovell, R. G., and Y. Ogura, 1989: Effect of vertical wind shear on numerically simulated multicell storm structure. *J. Atmos. Sci.,* **46,** 3144–3176.

Johnson, R. H., and D. L. Bartels, 1992: Circulations associated within a mature-to-decaying midlatitude mesoscale convective system. Part II: Upper-level features. *Mon. Wea. Rev.,* **120,** 1301–1320.

Jorgensen, D. P., and B. F. Smull, 1993: Mesovortex circulations seen by airborne Doppler radar within a bow-echo mesoscale convective system. *Bull. Amer. Meteor. Soc.,* **74,** 2146–2157.

——, M. A. LeMone, and S. B. Trier, 1997: Structure and evolution of the 22 February 1993 TOGA COARE squall line: Aircraft observations of precipitation, circulation, and surface energy fluxes. *J. Atmos. Sci.,* in press.

Keenan, T. D., and R. E. Carbone, 1992: A preliminary morphology of precipitation systems in northern Australia. *Quart. J. Roy. Meteor. Soc.,* **118,** 283–326.

——, and S. A. Rutledge, 1993: Mesoscale characteristics of monsoonal convection and associated stratiform precipitation. *Mon. Wea. Rev.,* **121,** 352–374.

Klemp, J. B., and R. B. Wilhelmson, 1978: The simulation of three-dimensional convective storm dynamics. *J. Atmos. Sci.,* **35,** 1070–1096.

——, and R. Rotunno, 1983: A study of the tornadic region within a supercell thunderstorm. *J. Atmos. Sci.,* **40,** 359–377.

Lafore, J.-P., and M. W. Moncrieff, 1989: A numerical investigation of the organization of the convective and stratiform regions of tropical squall lines. *J. Atmos. Sci.,* **46,** 521–544.

Leary, C. A., 1980: Temperature and humidity profiles in mesoscale unsaturated downdrafts. *J. Atmos. Sci.,* **37,** 1005–1012.

LeMone, M. A., 1983: Momentum transport by a line of cumulonimbus. *J. Atmos. Sci.,* **40,** 1815–1834.

——, G. M. Barnes, and E. J. Zipser, 1984a: Momentum fluxes by lines of cumulonimbus over the tropical oceans. *J. Atmos. Sci.,* **41,** 1914–1932.

——, ——, E. J. Szoke, and E. J. Zipser, 1984b: The tilt of the leading edge of mesoscale tropical convective lines. *Mon. Wea. Rev.,* **112,** 510–519.

Malkus, J. S., 1952: The slopes of cumulus clouds in relation to the external wind shear. *Quart. J. Roy. Meteor. Soc.,* **78,** 530–542.

McCaul, E. W., Jr., and M. L. Weisman, 1996: Simulations of shallow supercell storms in landfalling hurricane environments. *Mon. Wea. Rev.,* **124,** 408–429.

Rotunno, R., and J. B. Klemp, 1982: The influence of the shear-induced pressure gradient on thunderstorm motion. *Mon. Wea. Rev.,* **110,** 136–151.

——, ——, and M. L. Weisman, 1988: A theory for strong, long-lived squall lines. *J. Atmos. Sci.,* **45,** 463–485.

Roux, F., 1985: Retrieval of thermodynamic fields from multiple-Doppler radar data using the equations of motion and the thermodynamic equation. *Mon. Wea. Rev.,* **113,** 2142–2157.

——, J. Testud, M. Payen, and B. Pinty, 1984: West African squall-line thermodynamic structure retrieved from dual-Doppler radar observations. *J. Atmos. Sci.,* **41,** 3104–3121.

Rutledge, S. A., and P. V. Hobbs, 1984: The mesoscale and microscale structure and organization of clouds and precipitation in midlatitude cyclones. Part XII: A diagnostic modeling study of precipitation in narrow cold-frontal rainbands. *J. Atmos. Sci.,* **41,** 2949–2972.

Schlesinger, R. E., 1984: Effects of the perturbation pressure field in numerical models of unidirectionally sheared thunderstorm convection: Two versus three dimensions. *J. Atmos. Sci.,* **41,** 1571–1587.

Scott, J. D., and S. A. Rutledge, 1995: Doppler radar observations of an asymmetric mesoscale convective system and associated vortex couplet. *Mon. Wea. Rev.,* **123,** 3437–3457.

Skamarock, W. C., 1989: Truncation error estimates for refinement criteria in nested and adaptive models. *Mon. Wea. Rev.,* **117,** 882–886.

——, and J. B. Klemp, 1993: Adaptive grid refinement for two-dimensional and three-dimensional nonhydrostatic atmospheric flow. *Mon. Wea. Rev.,* **121,** 788–804.

——, M. L. Weisman, and J. B. Klemp, 1994: Three-dimensional evolution of simulated long-lived squall lines. *J. Atmos. Sci.,* **51,** 2563–2584.

Smull, B. F., and R. A. Houze Jr., 1987: Dual-Doppler analysis of a midlatitude squall line with a trailing region of stratiform rain. *J. Atmos. Sci.,* **44,** 2128–2148.

Szeto, K. K., and H.-R. Cho, 1994: A numerical investigation of squall lines. Part II: The mechanics of evolution. *J. Atmos. Sci.,* **51,** 425–433.

Thorpe, A. J., M. J. Miller, and M. W. Moncrieff, 1982: Two-dimensional convection in nonconstant shear: A model of midlatitude squall lines. *Quart. J. Roy. Meteor. Soc.,* **108,** 739–762.

Trier, S. B., and D. B. Parsons, 1995: Updraft dynamics within a numerically simulated subtropical rainband. *Mon. Wea. Rev.,* **123,** 39–58.

——, W. C. Skamarock, M. A. LeMone, D. B. Parsons, and D. P. Jorgensen, 1996: Structure and evolution of the 22 February 1993 TOGA COARE squall line: Numerical simulations. *J. Atmos. Sci.,* **53,** 2861–2886.

Verlinde, J., and W. R. Cotton, 1990: A mesoscale vortex couplet observed in the trailing anvil of a multicellular convective complex. *Mon. Wea. Rev.,* **118,** 993–1010.

Webster, P. J., and R. Lukas, 1992: TOGA COARE: The Coupled Ocean–Atmosphere Response Experiment. *Bull. Amer. Meteor. Soc.,* **73,** 1377–1416.

Weisman, M. L., 1992: The role of convectively generated rear-inflow jets in the evolution of long-lived mesoconvective systems. *J. Atmos. Sci.,* **49,** 1826–1847.

——, 1993: The genesis of severe long-lived bow echoes. *J. Atmos. Sci.,* **50,** 645–670.

——, and J. B. Klemp, 1984: The structure and classification of numerically simulated convective storms in directionally varying wind shears. *Mon. Wea. Rev.,* **112,** 2479–2498.

——, ——, and R. Rotunno, 1988: Structure and evolution of numerically simulated squall lines. *J. Atmos. Sci.,* **45,** 1990–2013.